High Q-factor Optical Resonances in the Elastic Scattering from Silicon Microspheres

by

Mohammed Sharif Murib

A Thesis Submitted to the
Graduate School of Sciences and Engineering
in Partial Fulfillment of the Requirements for
the Degree of

Master of Science
in
Physics

Koç University

July 2009

Koç University

Graduate School of Sciences and Engineering

This is to certify that I have examined this copy of a master's thesis by

Mohammed Sharif Murib

and have found that it is complete and satisfactory in all respects,
and that any and all revisions required by the final
examining committee have been made.

Committee Members:

_____

Ali Serpengüzel, Ph. D. (Advisor)

_____

Alper Kiraz, Ph. D.

_____

Kaan Güven, Ph. D.

Date: _____

ABSTRACT

The whispering gallery modes resonators have received increased attention as novel structures, which are suitable for various applications in linear, nonlinear and quantum optics. Small mode volumes and high optical quality factors are unique features of these resonators. These properties make possible high concentration of optical fields and relatively long photon confinement times. The spherical cavities confine light by total internal reflection at the inner surface boundary. In this study, elastic light scattering intensity calculations at 90^{o} and 0^{o} for the transverse electric and transverse magnetic polarized light were performed at 1200 nm for a 50 μm radius and 3.5 refractive index silicon microsphere. The mode spacing between morphology dependent resonances was found to be 1.76 nm. The linewidth of the morphology dependent resonances was observed to be on the order of 10^{-2}, which leads to a quality factor on the order of 10^{5}. Experimentally, high quality factor optical resonances are obtained in the elastic scattering spectra from a silicon microsphere with a radius of 500 μm and refractive index of 3.48. The mode spacing between morphology dependent resonances was found to be 0.27 nm. The linewidths of the resonances were found to be of the order 10^{-4} nm, which leads to Q factors of 10^{6}. As a result, silicon microspheres could be used as a resonant cavity enhanced optoelectronic devices for near infrared wavelength region as well as other application in linear, nonlinear and quantum optics.

ÖZET

Mikroçınlaçlar, doğrusal, doğrusal olmayan ve kuantum optik alanındaki eşsiz uygulamaları ile dikkat çekmektedirler. Küçük boyutları ve yüksek kalitedeki yapı tabanlı çınlamaları bu çınlaçların en önemli özellikleridir. Bu özellikler sayesinde çınlaçlar fotonları uzun süreler yerelleştirirler. Işık bu çınlaçlar içersinde tam geri yansıma ile iç yüzeyde yerelleşir. Bu çalışmada kırılma katsayısı 3.5 olan 50 μm yarıçapındaki silisyum mikroyuvarlar için esnek saçılma izgeleri 90^o ve 0^o de 1200 nm dalgaboyunda hesaplanmıştır. Yapı tabanlı kipler arasındaki mesafe 1.76 nm olarak hesaplanmıştır. Bu kiplerin çizgi genişliği 0.02 nm olarak bulunmuştur. Bu değerler ile kiplerin kalite faktörü 10^5 olarak bulunmuştur. Deneysel olarak, yüksek kalite faktörlü çınlamalar, esnek saçılma izgesinde 3.48 kırılma katsayısına sahip, 500 μm yarıçapındaki silisyum mikroyuvarlar için gözlemlenmiştir. Yapı tabanlı kipler arasındaki mesafe 0.27 nm olarak hesaplanmıştır. Bu kiplerin çizgi genişliği yaklaşık 10^{-4} nm olarak gözlemlenmiştir. Bu değerler ile kiplerin kalite faktörü 10^6 olarak bulunmuştur. Sonuç olarak, silisyum mikroyuvarlar doğrusal, doğrusal olmayan ve kuantum optik uygulamalarına ek olarak çınlaç zenginleştirilmiş optoelektronik aygıtlar olarak yakın kızılaltı dalgaboylarında kullanılabillir.

ACKNOWLEDGEMENTS

I am especially indebted to my advisor Prof. Ali Serpengüzel, who has dedicated considerable time and thought for academic support, supervision, and motivation during my research with endless tolerance and patience.

A special thank for Prof. Alper Kiraz and Prof. Kaan Güven for their help and their acceptance to be in the thesis committee of my master degree.

I would like to thank Prof. Oğuzhan Gürlü for his help at the Microphotonics Research Laboratory.

A deep thank for my partner at Microphotonics Research Laboratory, Emre Yüce, for his help and brotherhood.

A deep thank for Ersin Alpan, Hasan Yılmaz, Ersin Huseyinoglu, Kurt Webb, Selman Tamer, and Yiğit Uysallı for their close friendship.

I also wish to thank all my friends at Koç University and Microphotonics Research Laboratory for their support and help during my study.

My profound and continuous thank is for my parents, and sisters, for their great patience, tolerance, encouragement and support during all my life and to whom, I dedicate this thesis.

I would like to acknowledge the partial support of this research by the EC Grant Nos. FP6-IST-003887 NEMO, FP6-IST-511616 PHOREMOST and TUBITAK Grant No. EEEAG-106E215.

TABLE OF CONTENTS

LIST OF FIGURES

LIST OF TABLES

NOMENCLATURE

a	Radius of the sphere
b	Impact parameter
$\Delta\lambda$	Mode spacing in wavelength
Δx	Mode spacing in size parameter
Δx_p	Mode spacing in size parameter between TE and TM modes
$\delta\lambda$	Full width half maximum or linewidth in wavelength
ε	Permittivity of the medium
k	Imaginary part of refractive index
l	Radial mode order
l	path length inside a material
λ	Wavelength of light in vacuum
m	Azimuthal angular mode number
m	Real part of refractive index
μ	Permeability of the medium
n	Complex refractive index
n	Polar angular mode number
Q	Quality factor of a MDR
σ_{MDR}	Scattering cross section of a MDR
σ_{total}	Total scattering cross section
τ	Lifetime of photons in an MDR
ω_o	Half width of the Gaussian beam
ω	Optical angular frequency
x	Size parameter of the microsphere
MDR	Morphology dependent resonance

WGM	Whispering gallery mode
WDM	Wavelength division multiplexing
α	Absorption coefficient
α_{ss}	Surface scattering loss coefficient
α_{rad}	Radiative loss coefficient
α_{mat}	Material loss coefficient
$\alpha_{coupler}$	Coupling loss coefficient
VOA	Variable optical attenuater

Chapter 1

INTRODUCTION

The light, we see, reaches our eyes in an indirect way. Looking at a cloud, or at the sky, we see scattered sunlight. Scattering is often accompanied by absorption. A leaf of a tree looks green, because the leaf scatters the green light and absorbs the red and blue light. The red and blue light energy is converted to heat and are no longer present. Both scattering and absorption remove energy from a beam of light traversing the medium. The extinction is seen, when we look directly at the light source [1]. Therefore, we can define extinction as the sum of scattering and absorption,

$$\text{Extinction} = \text{Scattering} + \text{Absorption} \tag{1.1}.$$

The light scattering and absorption properties of particles help determine the color of paints, the distance a laser beam can propagate throught the atmosphere, the light induced motion of illuminated particles, and the enhancement of Raman scattering near metal particles [2].

Scattering and absorption phenomena can be utilized in instrumentation for optical particle characterization, filters and sun glasses, in which particles absorb and scatter

different colors of light, and in nonlinear optical devices such as cw silicon Raman lasers[3] with electronic modulation capability [4], and silicon lossless light modulators [5], in which particles may be used to enhance local fields [2]. Microspheres belong to the same group of interferrometric devices as Fabry-Perot interferometers and fiber Bragg gratings. The optical resonances in microspheres depend on the geometry (size and shape) and the refractive index of the microspheres.

Chapter 2 includes a brief description of silicon microspheres. The importance of silicon photonics and the recent achievements and applications in that field are presented. Moreover, there is a brief summary about the recent studies and applications done on silicon microspheres.

The general problem of light scattering by microspheres is illustrated in Chapter 3, which includes an overview of the elastic light scattering phenomena from a spherical particle as well as an explanation of the theory of morphology dependent resonances and the principle of their excitation. In addition, the special Lorenz-Mie theory (LMT) and the Generalized Lorenz-Mie theory (GLMT) are described briefly showing the external elastic scattering field coefficients equations.

Chapter 4 includes the calculations done for a silicon microsphere in the 1200 nm wavelength region. Elastic scattering intensity at 90^o and 0^o for the transverse electric (TE) and transverse magnetic (TM) polarization was calculated for a silicon sphere of radius 50 μm and refractive index of 3.5. This calculation showed the possibility of using a silicon

microsphere as a resonant cavity enhanced optoelectronic device for the near infrared wavelength region.

Chapter 5 shows the high quality factor optical resonances obtained in the elastic scattering spectra from a silicon microsphere with a radius of 500 μm and refractive index of 3.48 coupled to an optical fiber half coupler. The mode spacing between morphology dependent resonances was found to be 0.27 nm. The linewidths of the resonances were found to be of the order 10^{-4} nm, which leads to Q factors of 10^{6}.

Chapter 6 concludes with a summary of the thesis work as well as the outlook for future work.

The appendix describes the mounting of a standard telecom laser operating at 1300 nm in a homemade laser diode head with thermal and electrical control.

Chapter 2

SILICON MICROSPHERE

2.1 Silicon Photonics

Photonics is the technology of emission, transmission, control and detection of light using fiber optics and optoelectronic devices. Silicon photonics concentrate on photonic devices that have silicon as the base material. Silicon photonics originated around 1980's [6-9]. Early success was in passive devices in the 1990's [9-16]. The success of silicon is due to its wide availability, and purification to an unprecedented level [17]. Silicon can also be handled and manufactured easily, and shows very good thermal and mechanical properties, which facilitate the fabrication of the devices based on silicon [17]. Silicon has suitable material properties for photonic devices such as high thermal conductivity (10 x higher than GaAs), high optical damage threshold (10 x higher than GaAs), and high third order optical nonlinearities [18]. Silicon photonics is proceeding towards mass manufacturing of discrete optical components, integrated transceivers for synchronous optical network, gigabit ethernet, and optical backplane markets [18]. A recent commercial silicon photonic based device, the eight channel variable optical attenuator (VOA), was produced recently [19]. Another prototype device, a four channel wavelength-division

multiplexing (WDM) transceiver was also reported [19]. Another mainstream envisioned for silicon photonics is optical interconnects for complementary metal oxide semiconductor (CMOS) electronics [20]. Silicon photonics can also be used in biosensing applications [18]. Another advantage of silicon is its bandgap energy of 1.1 eV, which makes silicon transparent in the optical communication wavelengths greater than 1.1 μm [21].

Silicon photonics had the challenge to create a light emitting device on crystalline silicon due to the indirect bandgap of crystalline silicon [18]. Consequently, light emission in silicon was created by using silicon engineered materials such as erbium-doped silicon-rich oxides [18].

2.2 RESONANT CAVITY ENHANCED DETECTOR

The increase in data rates of interchip communication, and the development of high speed fiber optic communication create a demand for high speed photodetectors. Commercially available fast photodetectors such as Schottky photodiodes have bandwidths exceeding 200 GHz [22]. The efficiency of conventional high speed photodetectors is limited due to the thin absorption region needed for short transit times of the photocarriers [22]. A high efficiency photodetector needs to have a thick active region, which would have the drawback of an increase in the transit time of the photogenerated carriers and a decrease in the speed of the device [23]. For a photodetector to have a high bandwidth and high speed,

the transit time of the photogenerated carriers within the depletion region must be small for a limited thickness of the absorption layer [23].

A solution to achieve an efficient high speed photodetector with a thin absorbing layer is the resonant cavity enhanced (RCE) device [24, 25]. RCE detectors operate at high speed, and have a thin absorbing region, which decreases the transit time of the photogenerated carriers [26]. RCE detectors detect light at the resonant wavelength of the cavity and reflect the nonresonant wavelengths [26]. The RCE photodetector consists of a thin absorbing layer set within a Fabry-Perot cavity [23] as shown in figure2 [25]. Once the device is illuminated and the resonance condition is fulfilled, the internal optical field amplitude will be enhanced [27].

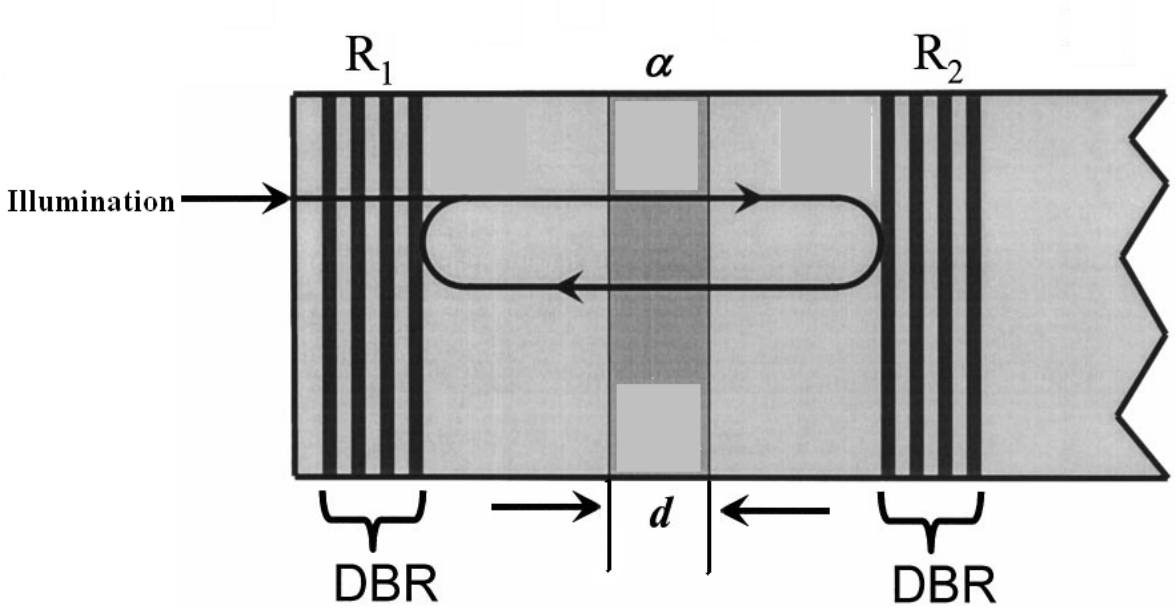

Figure 2.1: Cross section of Fabry-Perot cavity with distributed Bragg reflectors (DBR's). d and α are the absorbing layer thickness and absorption coefficient, respectively.

Silicon based photodetectors are able to monolithically integrate detectors [25]. Si-RCE photodetectors have been shown to provide high bandwidths [25]. Si-RCE photodetectors have low dark currents on the order of picoamperes, which is an advantage of Si over III-V devices [28]. In addition to Si-RCE photodetectors, silicon based devices can be used for communication systems, optical bus systems for ultra large scale integrated (ULSI) circuits, and I/O stages for system-on-a-chip (SOC) [28].

2.3 Optical Losses in Silicon

According to the Beer-Lambert law for light absorption in the absence of nonlinear optical processes (figure 2.2), the intensity of light as a function of the distance traveled (l) through the material and absorption coefficient (α) is given by

$$I(l) = I_o\, e^{-\alpha l} \qquad \textbf{(2.1),}$$

where I_o is the incident light intensity.

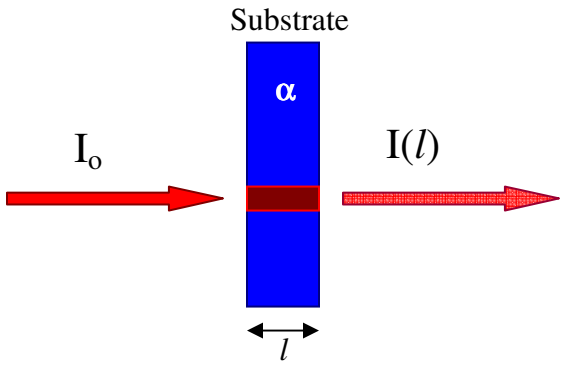

Figure 2.2: Beer-Lambert absorption of a beam of light penetrating a substrate of thickness l.

The optical absorption coefficient, (α) the attenuation caused by [30] material losses (α_{mat}). Surface scattering is induced by the imperfections of the surface. Material losses are caused by the fundamental absorption in the material, atomic impurities and the three types of bulk scattering: Raman, Brillouin, and Rayleigh.

The variation of the absorption coefficient (α) of a silicon substrate of thickness 600 μm and refractive index 3.5 is shown in figure 2.3 [34].

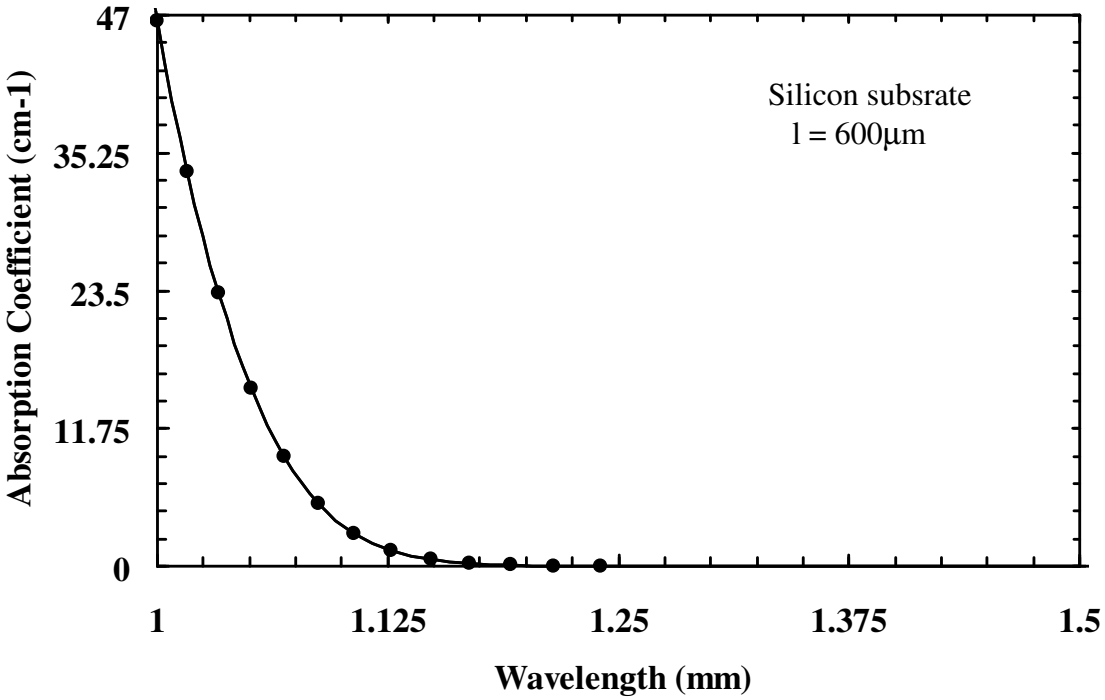

Figure 2.3: Absorption coefficient of silicon wafer 600mm thick versus wavelength.

Figure 2.3 shows that the absorption coefficient decreases gradually with the increase in the wavelength until 1.245 μm, where silicon no more absorbs and the absorption

coefficient becomes null at wavelength greater than 1.25 μm. Consequently silicon becomes transparent at wavelengths greater than 1.25μm.

2.4 Silicon Microsphere

Microspheres have received increasing attention as optical microcavity resonators due to their high quality morphology dependent resonances (MDR's) [29]. Silicon microspheres with their MDR's are a new paradigm for the use of silicon in optical communication applications [30]. Recent studies were done for spherical silicon solar cells [31], near-IR communication applications [32], and for electrophotonic integration [33]. In this case the material and the cavity are combined into monolithic silicon microsphere. A scanning electron micrograph (SEM) of a silicon microsphere of radius 0.5 mm and refractive index of 3.48 is shown in figure 2.4.

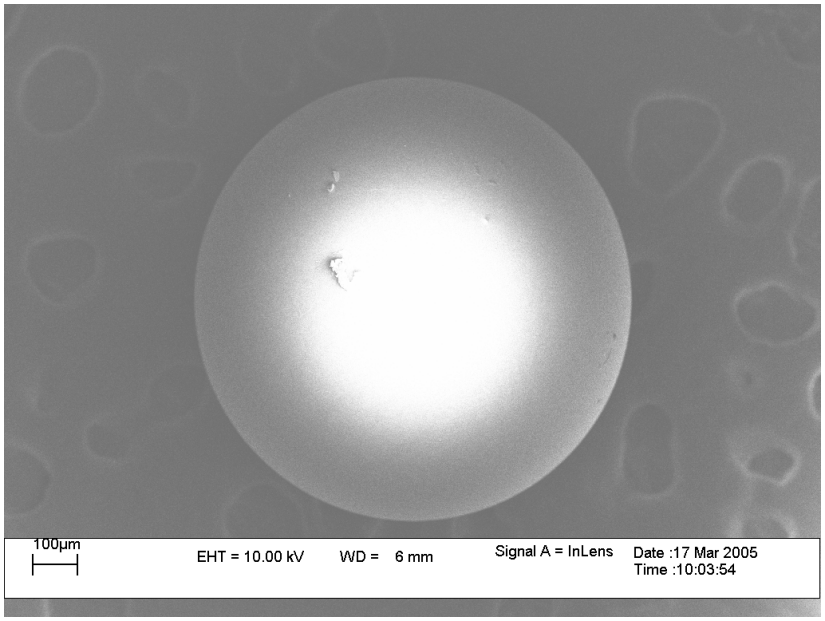

Figure 2.4: Scanning Electron Micrograph (SEM) of a silicon sphere of radius 0.5 mm.

The number of possible roundtrips is given by

$$\text{Number of roundtrips} = \frac{1}{2\pi a\alpha} \qquad \textbf{(2.2)},$$

where a is the radius of the sphere, and α the absorption coefficient. The possible number of roundtrips of trapped light in a silicon sphere of radius 500 μm and refractive index 3.48 as a function of wavelength is shown in figure 2.5.

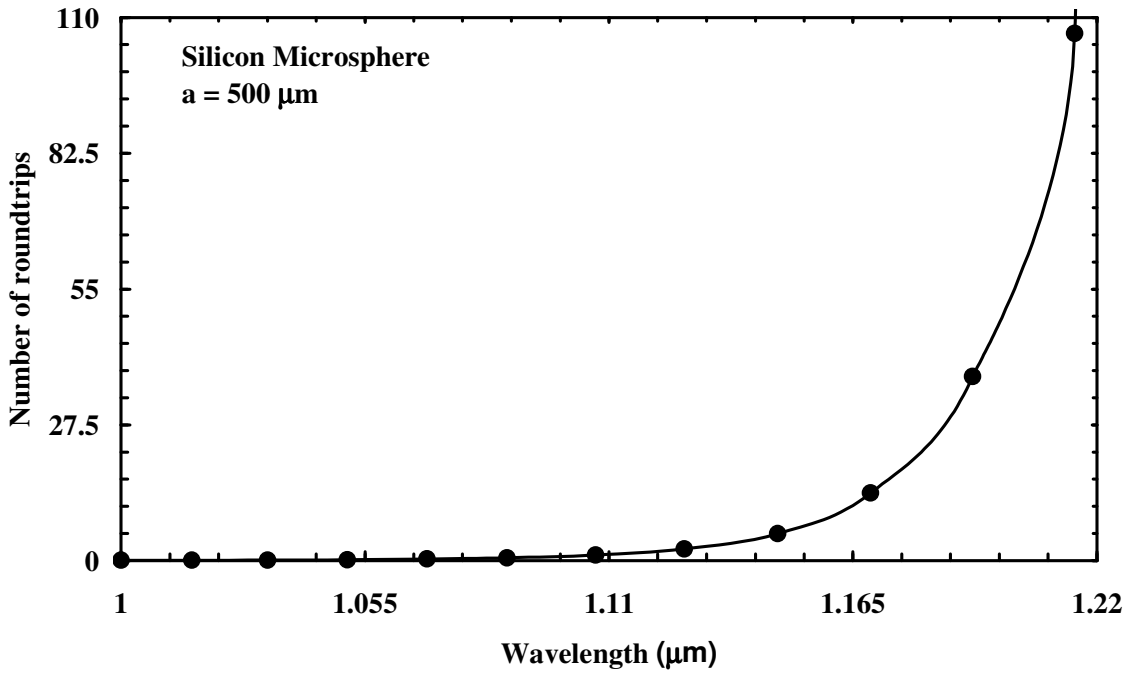

Figure 2.5: Number of round trips in a silicon sphere of radius 0.5 mm in the range 1.1-1.22μm.

Figure 2.5 shows the possible number of roundtrips of trapped light in the same sphere as a function of wavelength in the range 1-1.22 μm. Because the absorption coefficient becomes zero above 1.25 μm, then the number of round trips increases as wavelength increases as shown in figure 2.6.

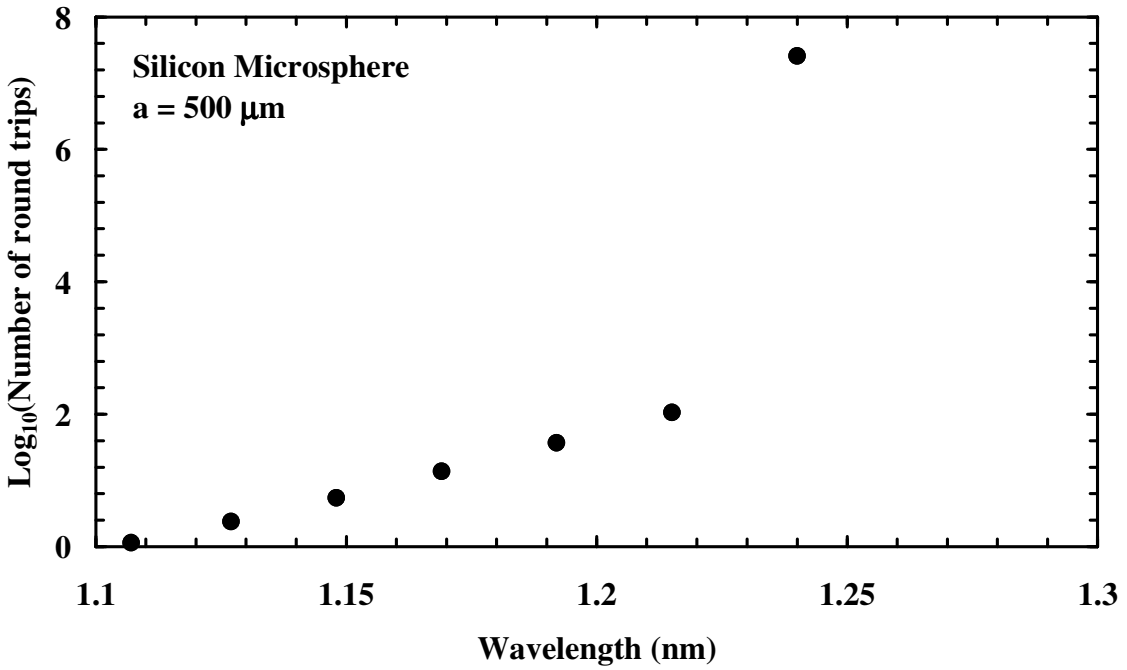

Figure 2.6: logarithmic scale of the number of round trips in a silicon sphere of radius 0.5 mm in the range 1.1-1.3 μm.

The trapped light inside the sphere is expected to make around 25×10^6 turns at 1.25 μm before all of the light is absorbed. At wavelengths greater than 1.25μm, the trapped light inside the sphere is expected to make a large number of turns before the light is absorbed.

Chapter 3

ELASTIC LIGHT SCATTERING FROM SPHERICAL MICROPARTICLES

3.1 Overview

Microspheres have attracted the attention of the optical spectroscopy community in the recent years due to their unique optical properties [35]. The interface of the sphere causes three electromagnetic and quantum electrodynamic effects to take place [36]. At a specific wavelength, which satisfies the morphology dependent resonance (MDR) condition, the microsphere behaves as an optically resonant cavity [36]. MDRs can be considered as standing waves that can be decomposed into two counterpropagating waves circumnavigating the microsphere [36]. Also as a result of the modified density of the final electromagnetic states, the transition cross sections in the microsphere are larger than the same in a bulk transition cross section [37]. In the microsphere, the final states correspond to MDRs whereas in the bulk, the final states are the continuum modes of an infinite system [38, 39].

3.2 Scattering Geometry

Figure 3.1 shows an incident electric field, E_{input}, illuminating a sphere of radius a. Some fraction of E_{input} is scattered by the sphere, and is denoted as $E_{scattered}$. The elastically scattered light has the same frequency as the incident light. Inelastically scattered light due to the Raman effect and quantum transitions are excluded.

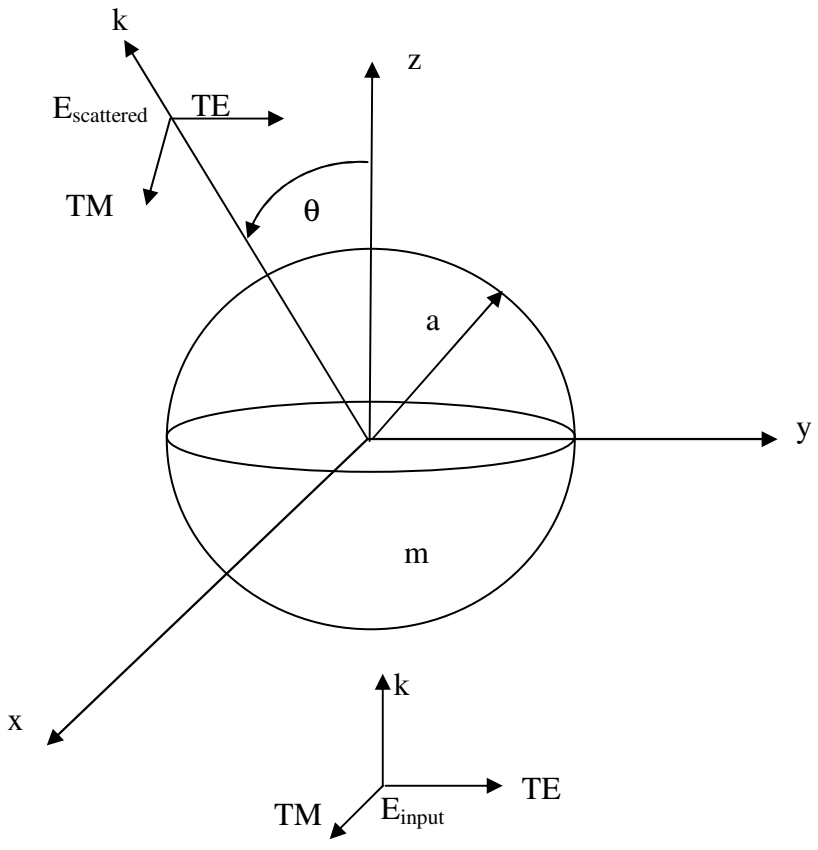

Figure 3.1: Geometry of a sphere of radius a illuminated by a plane wave propagating in the +z direction.

3.3 Scattering Cross-section

The intensity is the most important property of the scattered wave [1]. The intensity is defined as the power per unit area. At any point in the distant field, the incident wave and the scattered wave are confined to a direction or to a solid angle around this direction [1]. The incident and the scattered light are characterized by their intensity, polarization, and phase. The phases cannot be measured directly, but are of importance in the full formulation of the scattering of polarized light [1]. The scattered wave at any point in the distant field has the character of a spherical wave, in which energy flows outward from the particle. The direction of the scattering wave from a particle to any point in the distant field is characterized by the polar angle θ and the azimuthal angle ϕ, relative to the direction of propagation of the incident light [1]. The scattered intensity ($I_{scattered}$) can be calculated as [1]

$$I_{scattered} = \frac{I_{input} F(\theta, \varphi)}{k^2 r^2} \quad \textbf{(3.1),}$$

where I_{input} is the incident intensity, k the wave vector, and $F(\theta,\varphi)$ a dimensionless function of the direction but not of r, which depends on the orientation of a particle with respect to the direction of the incident wave. In our case, the orientation of the particle is irrelevant due to the sphere's symmetry in ϕ, and F is a function of θ only.

If we let the total energy scattered in all directions be equal to the energy of the incident wave falling on the area $C_{scattered}$

$$C_{scattered} = \frac{1}{k^2}\int F(\theta,\varphi)\sin\theta d\theta d\varphi \quad \textbf{(3.2),}$$

The extinction cross-section is equal to the sum of the scattering cross-section and the absorption cross-section and can be calculated as

$$C_{extinction} = C_{scattered} + C_{absorbed} \quad \textbf{(3.3).}$$

For non absorbing spheres since $C_{absorbed} = 0$, we have $C_{extinction} = C_{scattering.}$

3.4 Morphology Dependent Resonances

When the size of regularly shaped particles such as spheres become comparable to the wavelength of light, the optical field intensity near the surface is enhanced and becomes many times greater than that of the incident intensity [40]. A nonlinear material response can occur for a very long time, which opens new perspectives in quantum electrodynamics [41]. The elastic light scattering spectra are based on the optical geometry of the sphere. The electromagnetic wave energy is trapped inside the silicon microsphere as it propagates around the inside surface by an almost total internal reflection [42]. After the circumnavigation of the electromagnetic wave in the sphere, the resonating light manifests a series of sharp peaks (MDRs) each as a function of the sphere's size parameter [42].

The optical resonances of a microsphere depend on the geometry, size, and relative refractive index of the material to the medium [43]. Any variation in the size or the relative refractive index corresponds to a shift in the MDRs.

3.5 Plane Wave or Gaussian Beam Illumination

When the sphere is illuminated with a plane wave (figure 3.2), the internal intensity is concentrated along the principal diameter near the front and the back surfaces of the microsphere [36].

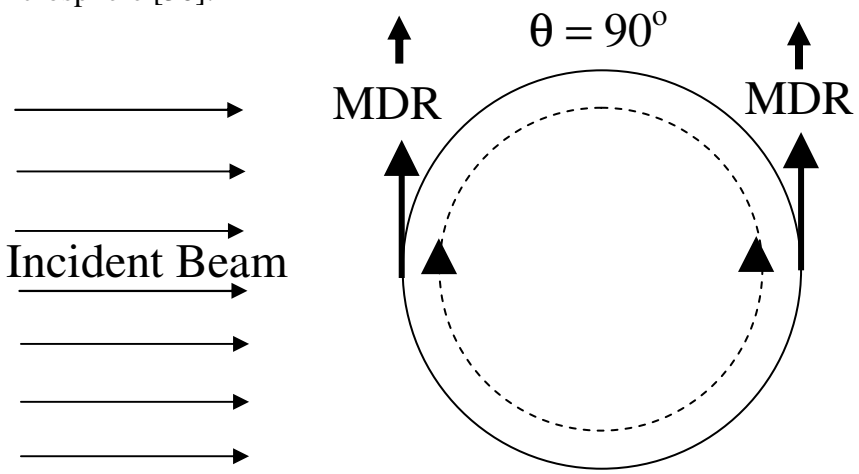

Figure 3.2: Schematic of the side view of a microsphere illuminated with a plane wave and exciting MDRs.

When the incident plane wave is resonant, a uniform intensity distribution, on the optical axis around the edge of the sphere, in the volume determined by the MDRs, will be created [44]. If an off-axis Gaussian beam is sent to the sphere on a resonant frequency as in figure 3.3, then the internal intensity distribution will be all within the edge of the sphere, on the

optical axis, in the volume determined by the MDR and is no longer concentrated near the front and the back surfaces of the sphere [45].

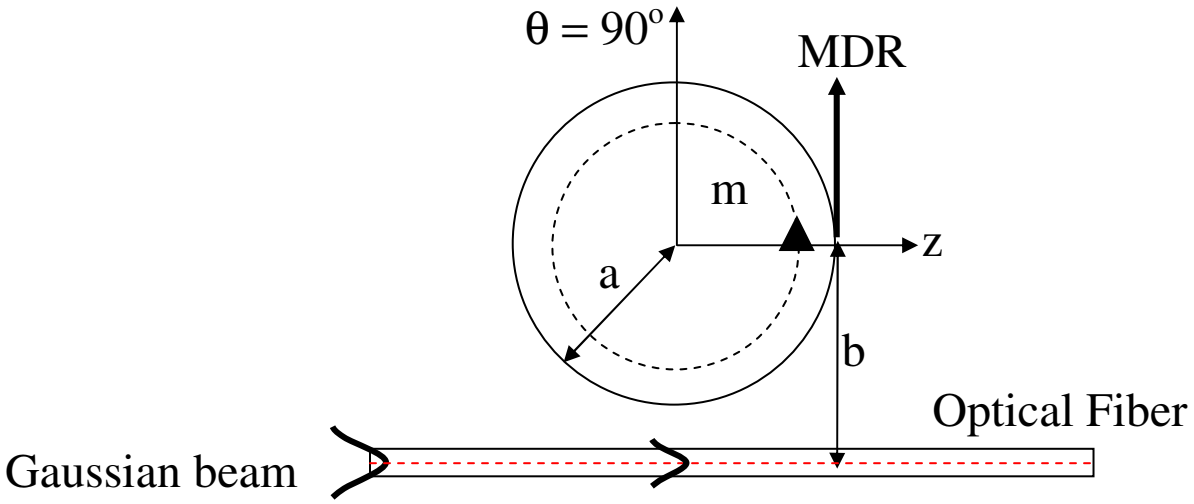

Figure 3.3: Schematic illustration of a silicon microsphere coupled to an optical fiber placed at an impact parameter b away from the sphere center

Another advantage for the Gaussian beam is that, an edge illumination with a focused beam excites MDRs more efficiently than does a plane wave [46, 47]. Moreover, if one is interested in a phenomenon that needs the existence of an incident light on only one small part of the spherical particle, most of the plane energy is wasted because it strikes the particle at the wrong place.

3.6 MDR Analysis

A number of theoretical studies have been performed about MDR's, which are also known as whispering gallery modes (WGMs) [42]. There are three different analytical explanations for the MDR phenomenon. The first analysis uses Maxwell's equations for an incident electromagnetic wave on a resonating cavity [48-50]. In a homogeneous sphere, the electromagnetic wave is expressed in terms of spherical coordinates [51-53]. The Maxwell's equations solutions in spherical coordinates for the MDR process have been described in the literature [54]. Polarized electromagnetic fields were introduced as a result of the analytical techniques derived from the solution of Maxwell's equations [54]. A quantum mechanical analogy between the scalar Helmholtz's equation that results from solving the Maxwell's equations in spherical coordinates and the Schrödinger's equation was a second explanation for MDR's [55]. A Shrödinger-like equation and the analogy with the hydrogen atom have brought into the picture the new concept of the photonic atom model [56].

This quantum mechanical approach suggests that energy is trapped near the surface of a microsphere [57]. Coupling is due to tunneling through the outer wall. The third explanation for the MDR phenomenon includes a geometric optics approach, which is attractive due to its simplicity and straight forward explanation of the physical phenomenon [57, 58].

To simplify, the MDR phenomenon, when an electromagnetic wave is coupled to a sphere, the field components' intensity distribution inside follow the solutions of the scalar Helmholtz's equation in spherical coordinates [51, 52]. These intensity distributions are called eigenfunctions or modes. The equations resulting from the solutions of the Helmholtz's equation are functions of the sphere's geometrical and material properties. As a result the distributions of the intensities inside the sphere are affected. In addition, the sphere acts as a resonator by responding more strongly to some electromagnetic fields than others [53].

The solutions of the scalar Helmholtz's equation in spherical coordinates are the radial, azimuthal and polar eigenfunctions, which are associated with the radial (l), polar (n), and azimuthal (m) mode numbers [59]. The radial modal number l gives the number of nodes of the intensity distribution in the radial direction. The radial mode number (l) can take the values between 1 and l_{max}. The maximum radial mode number (l_{max}) is given by the equation [60]

$$l_{max} = \frac{x}{\pi}\left[\frac{8}{9}\frac{(m-1)^3}{m}\right]^{\frac{1}{2}} + \frac{1}{4} \qquad (3.4).$$

The polar mode number n is approximately the number of wavelengths packed around the circumference of the resonator traveling around the sphere's great circles. The polar mode number n can take the values $x \le n \le mx$ [61]. The azimuthal mode number m can take the values $0 \le m \le n$ [61].

3.7 Specialized Lorenz-Mie Theory (SLMT)

Lorenz and Mie have expressed the equations for the scattered fields of a linearly polarized electromagnetic plane wave of wavelength λ by a homogeneous sphere of radius a and complex refractive index m in terms of an infinite series of spherical multipole partial waves n [**62**]. The two polarization states transverse magnetic (TM) and transverse electric (TE) of each partial wave have the scattering amplitudes a_n and b_n respectively corresponding in the $a >> \lambda$ limit,

$$a_n = \frac{j_n(x)\left[mx\, j_n(mx)\right]' - m^2 j_n(mx)\left[x\, j_n(x)\right]'}{h_n^{(2)}(x)\left[mx\, j_n(mx)\right]' - m^2 j_n(mx)\left[x\, h_n^{(2)}(x)\right]'} \qquad (3.5),$$

$$b_n = \frac{j_n(x)\left[mx\, j_n(mx)\right]' - m^2 j_n(mx)\left[x\, j_n(x)\right]'}{h_n^{(2)}(x)\left[mx\, j_n(mx)\right]' - j_n(mx)\left[x\, h_n^{(2)}(x)\right]'} \qquad (3.6),$$

where the prime ($'$) stands for the derivative with respect to the argument [63], $j_n(x)$ is the spherical Bessel function of the first kind, $h_n^{(2)}(x)$ is the Hankel function of the second kind, x is the size parameter ($x = 2\pi a/\lambda$), m is the refractive index. The MDRs of the microsphere appear for the wavelengths that makes the denominators of a_n and b_n approache zero, that is at the poles of the coefficient equations [64].

3.8 Generalized Lorenz-Mie Theory (GLMT)

The Generalized Lorenz-Mie theory (GLMT) expresses the equations for the scattered fields of a transversally localized (focused) beam such as Gaussian beam of wavelength λ by a homogeneous sphere of radius a and complex refractive index m in terms of an infinite series of spherical multipole partial waves (n) with specified coefficients [60],

$$b_{nm} = b_n B_n^m \tag{3.7},$$

$$B_n^m = \frac{a^2}{n(n+1)\psi_n(x)} \int_0^{4\pi} d\Omega H_r(\Omega) Y_{nm}^*(\Omega) \tag{3.8},$$

where $Y_{nm}^*(\Omega)$ is the spherical function, $\psi_n(x)$ is the Ricatti-Bessel function, and $H_r(\Omega)$ is the radial component of magnetic field incident on the sphere surface. B_n^m is the beam shape coefficient. Knowing the beam shape coefficients is crucial to GLMT, since the scattered intensity and all the quantities derived from the scattered intensity are written in

terms of combinations of the beam shape coefficients, the plane wave partial wave scattering amplitudes a_n and b_n of the SLMT and the angular functions [62].

3.9 Quality Factor

The quality factor (Q) of a resonance is defined as [3]

$$Q = \frac{2\pi \,\text{Stored Energy}}{\text{Energy lost per cycle}} \qquad \textbf{(3.9).}$$

Also the quality factor (Q) provides the information about the average lifetime of a photon in the resonant mode, which is given by [35]

$$\tau = \frac{Q}{\omega_0} \qquad \textbf{(3.10),}$$

where ω_o is the resonant angular frequency.

The quality factor (Q) gives the number of cycles required for the stored energy to decrease to $e^{-\pi}$ of the original value [35]. In addition, Q gives information about the linewidth (Full Width Half Maximum) $\delta\lambda$ and is expressed by

$$Q = \frac{\lambda_o}{\delta\lambda} \qquad \textbf{(3.11).}$$

where λ_o is the resonant wavelength.

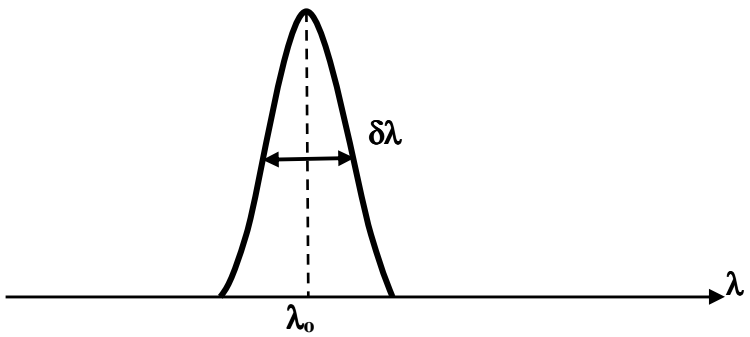

Figure 3.4: Illustration of a single MDR spectrum.

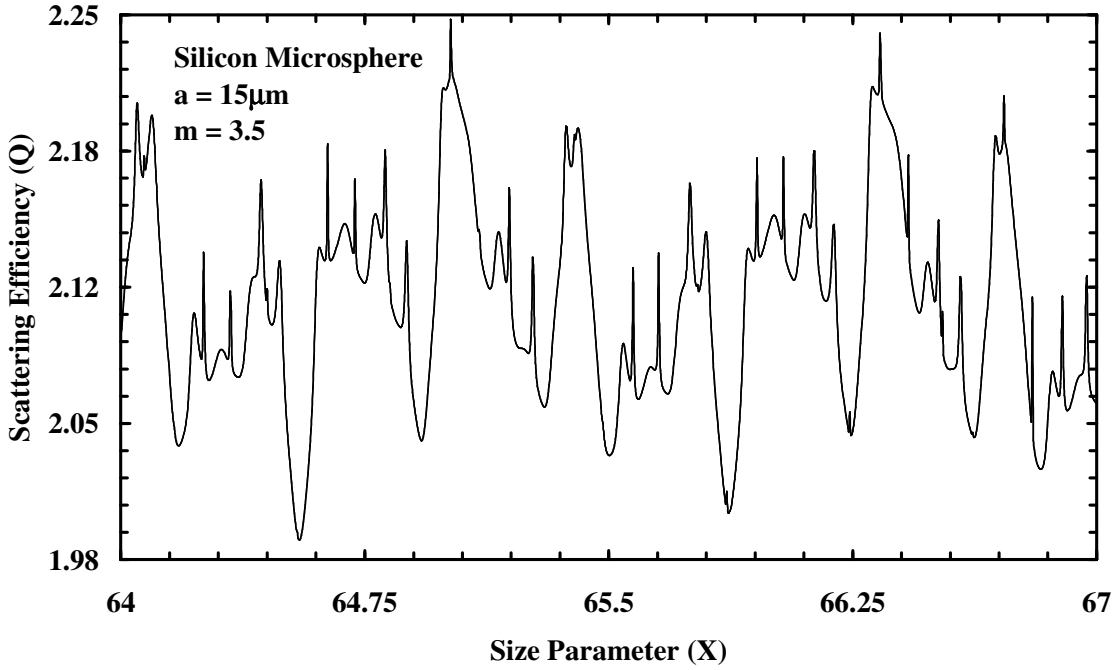

Figure 3.5: The variation of the resonances linewidth as a function of size parameter (x).

Figure 3.5 shows the calculated scattering efficiency of a sphere of refractive index m=3.5 as a function of the size parameter (x) using Steve Hill program [2]. The figure shows that the linewidth of the resonances become narrower as the sphere size increases.

3.10 Mode Spacing

The mode spacing ($\Delta\lambda$) is the spacing between the MDRs of the same mode number (n) and consecutive mode orders (l). The mode spacing is expressed by the equation [65]

$$\Delta\lambda = \frac{\lambda^2 \arctan\sqrt{(m^2-1)}}{2\pi a\sqrt{(m^2-1)}} \qquad \textbf{(3.12),}$$

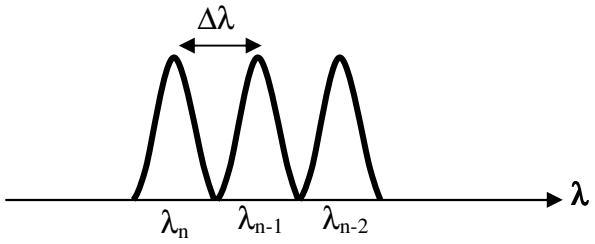

Figure 3.6: Schematic illustration of the mode spacing Δλ.

The mode spacing in size parameter (Δx) is

$$\Delta x = \frac{\arctan\sqrt{(m^2-1)}}{\sqrt{(m^2-1)}} \qquad \textbf{(3.13).}$$

where $x = \frac{2\pi a}{\lambda}$ is the size parameter.

The mode spacing between nearly identical TE and TM modes is expressed by [66]

$$\Delta x_p = \frac{\sqrt{(m^2-1)}}{m} \qquad \textbf{(3.14),}$$

where m is the refractive index.

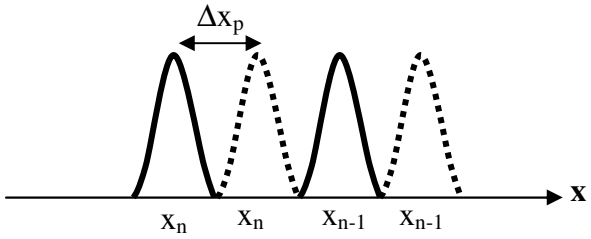

Figure 3.7: The mode spacing between nearly identical TE and TM modes, where the dashed lines represent the TM mode and the solid lines represent the TE mode.

3.11 Number of Resonances

The density of MDRs can be estimated by [35]

$$\frac{dN(x)}{dx} = \frac{x\rho^2\left(\rho - \tan^{-1}(\rho)\right)}{\pi} \tag{3.15},$$

where $\rho = (m^2 - 1)^{\frac{1}{2}}$. By substitution for N(λ) is found as

$$N(\lambda) = \int \frac{4\pi^2 a^2 \rho\left[\sqrt{\rho} - \tan^{-1}\sqrt{\rho}\right]d\lambda}{\pi\lambda^3} \tag{3.16}.$$

3.12 Excitation of Resonances in Microspheres

An external electromagnetic field can be used to excite the MDR's of a sphere. At optical frequencies, an incident laser beam can be coupled to the sphere by using an optical fiber half coupler by approaching the sphere as shown in Figure 3.5. The optical coupling between the sphere and the fiber can be facilitated by etching or heating and stretching the section of the fiber that is to be in contact with the sphere [67].

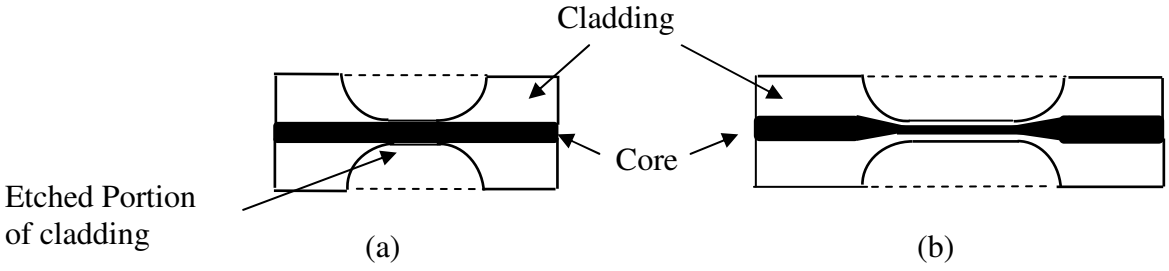

Figure 3.8: (a) Etching and (b) heating and stretching of the fiber.

In both cases, the evanescent field extends beyond the fiber boundary. A small diameter of the thinned fiber enables the positioning of a microsphere very close to the core of the fiber, and provides a better coupling of light into the sphere. In addition, since the core of a single mode fiber supports only one fundamental mode, with its evanescent field extending far beyond the core boundary, the etched fiber produces a cleaner coupling.

Chapter 4

THEORETICAL CALCULATIONS

Generalized Lorenz-Mie theory [68] is used to calculate the elastic scattering intensity at 90^o and 0^o for the transverse electric (TE) and transverse magnetic (TM) polarization for a silicon sphere of radius 50 μm and refractive index m=3.5 in the 1200 nm wavelength range. The mode spacing $\Delta\lambda$ between the morphology dependent resonances of same mode number and consecutive mode order was calculated to be 1.76 nm at λ = 1200 nm using equation 3.12. The absorption coefficient of silicon at 1200nm is $0.0298cm^{-1}$, which corresponds to an absorption length of 33 cm, which is greater than the circumference of the silicon sphere.

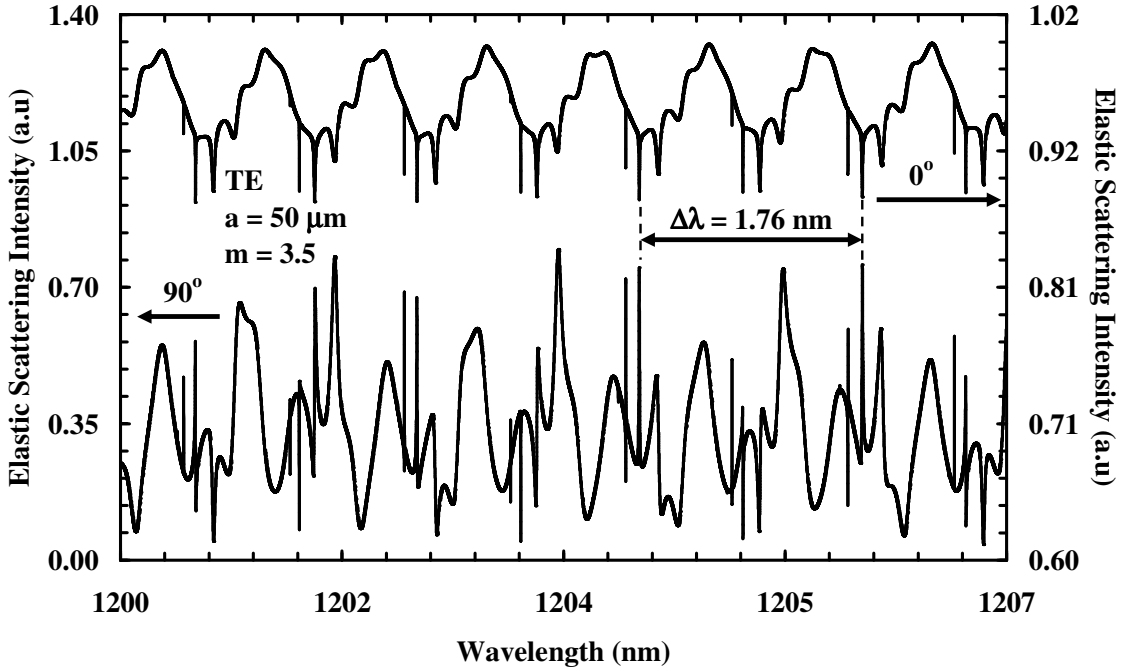

Figure 4.1: Low resolution transverse electric (TE) polarized elastic scattering spectra at 1200 nm

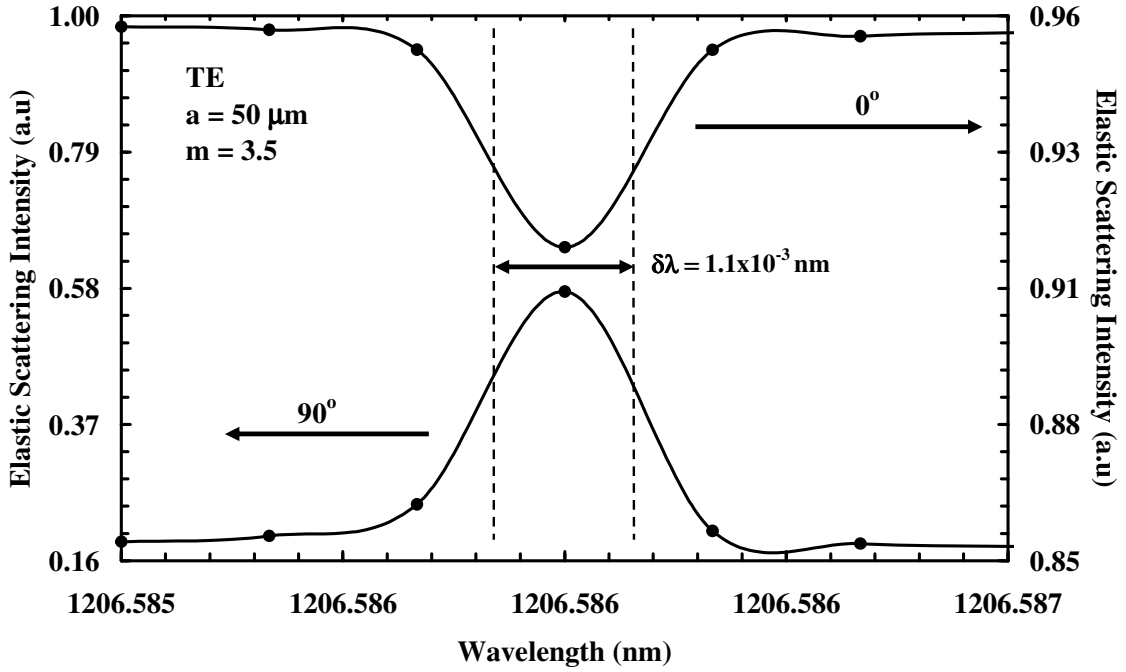

Figure 4.2: High resolution transverse electric (TE) polarized elastic scattering spectra at 1200nm.

Figure 4.1 shows the low resolution spectrum of the transverse electric (TE) polarized and figure 4.2 shows the high resolution spectrum of the (TE) polarized elastic scattering intensity in the 1200 nm range. The upper curve in figure 4.1 and figure 4.2 shows the elastic scattering intensity calculated for forward scattering at 0^o (transmission), and the lower curve shows the elastic scattering calculated for channel dropping at 90^o.

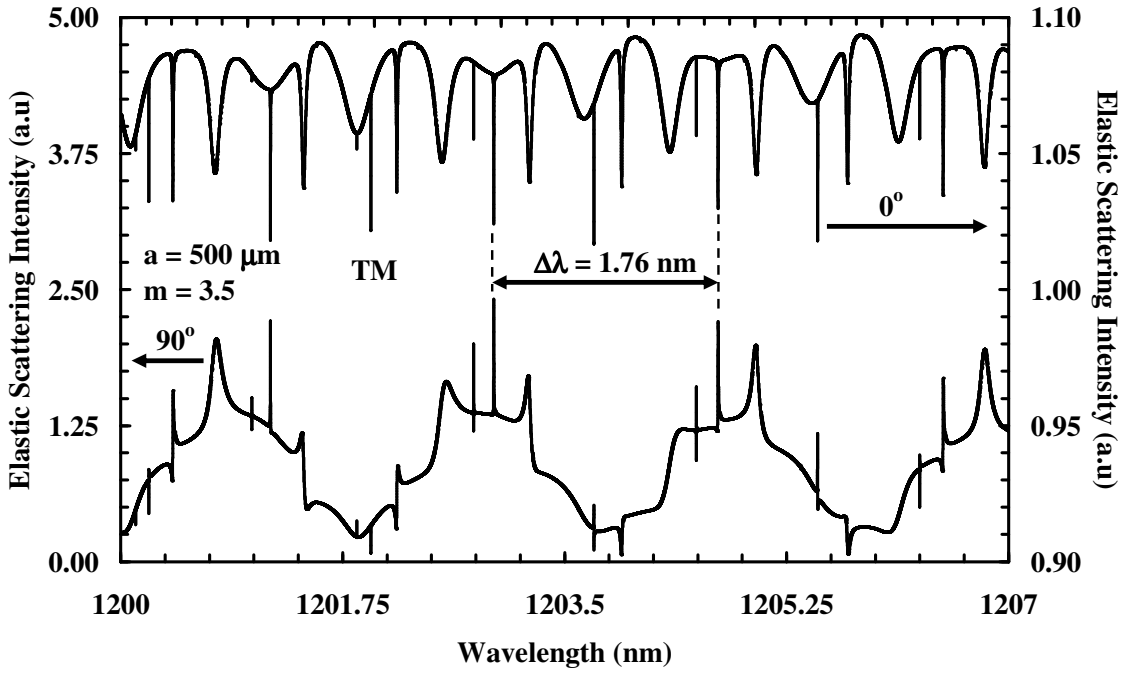

Figure 4.3: Low resolution transverse magnetic (TM) polarized elastic scattering spectra at 1200nm.

Figure 4.3 and 4.4 show the low resolution transverse magnetic (TM) polarized and high resolution TM polarized elastic scattering intensity respectively in the 1200 nm region. The upper curve in figures 4.3 and 4.4 show the transmitted intensity (elastic scattering at 0^o) and the lower curves show the channel dropping (elastic scattering at 90^o).

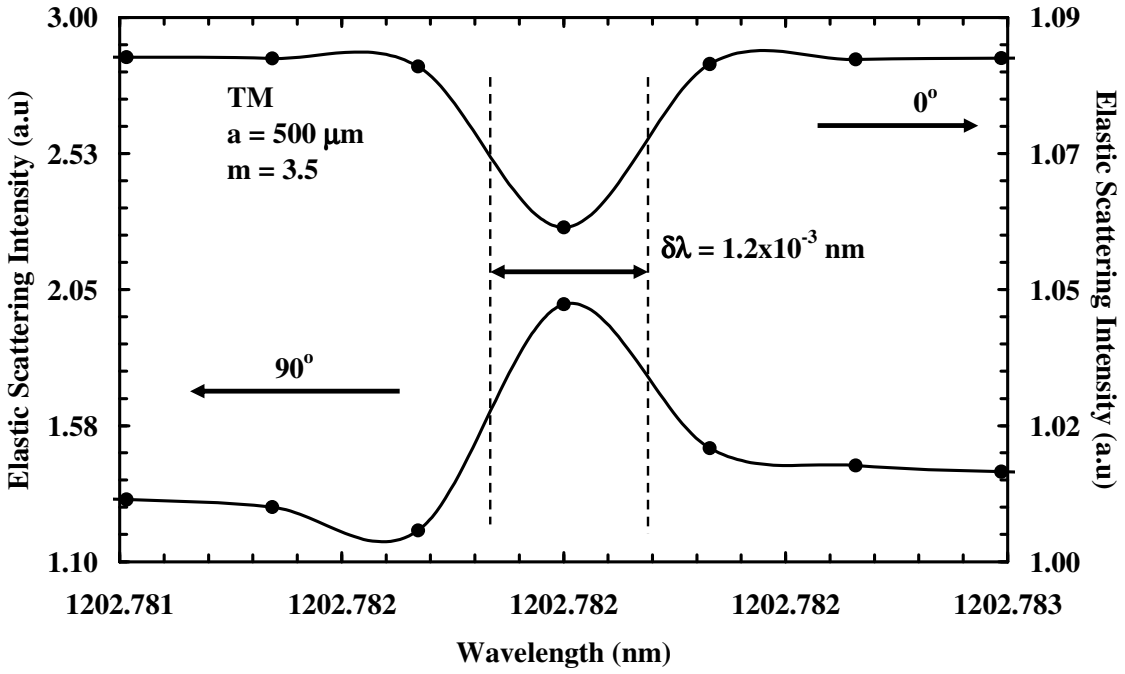

Figure 4.4: High resolution transverse magnetic (TM) polarized elastic scattering spectra at 1200nm.

In the TE and TM polarized spectra, the mode spacing ($\Delta\lambda$) is 1.76 nm. This correlates well with the optical size of the microsphere. The linewidth ($\delta\lambda$) of the MDRs shown in figures 4.2 and 4.4 is on the order of 10^{-3} nm, which corresponds to a Q on the order of 10^6. Due to the presence of multiple sets of transverse modes with different radial mode order (l), a multimode behavior is observed [59]. The transmission is not suitable for signal monitoring as the dips are only 3% of the maximum transmission intensity. On the other hand, the elastic scattering at 90^o has a larger dynamic range of about 41% of the maximum elastic scattering intensity, which leads to a relatively large interchannel crosstalk suppression [69].

Chapter 5

EXPERIMENTAL MEASUREMENTS

5.1 Introduction

High quality factor optical resonances are obtained in the elastic scattering spectra from a silicon microsphere with a radius of 500 μm and refractive index of 3.48. The mode spacing between morphology dependent resonances was found to be 0.27 nm. The linewidths of the resonances were on the order of 10^{-4} nm, which lead to Q factors of 10^{6}.

5.2 Experimental Setup

Figure 5.1(a) shows the schematic of the experimental setup. A tunable diode laser with a wavelength of 1473 nm is used in order to excite the MDRs of the silicon microsphere. In order to tune the wavelength of the diode laser, the laser temperature was tuned using a laser diode controller (LDC). The temperature of the laser was tuned from 14^{o}C to 16.2^{o}C at a constatnt current of 26.3 mA. The temperature corresponds to wavelength range of 1472.56-1473.42 nm. Elastic scattering light from the microsphere at 90^{o} was collected by a microscope lens and detected by an InGaAs photodetector. The polarization of the collected scattered light was controlled with a polarizer inserted between the InGaAs

photodiode detector and the microscope eyepiece lens as shown in figure 5.1(a) and 5.2 (b). The InGaAs photodiode signal was sent to a digital oscilloscope for signal monitoring and data acquisition. The transmitted power through the optical fiber is detected by an InGaAs power head (PWH) connected to the optical multimeter (OMM).

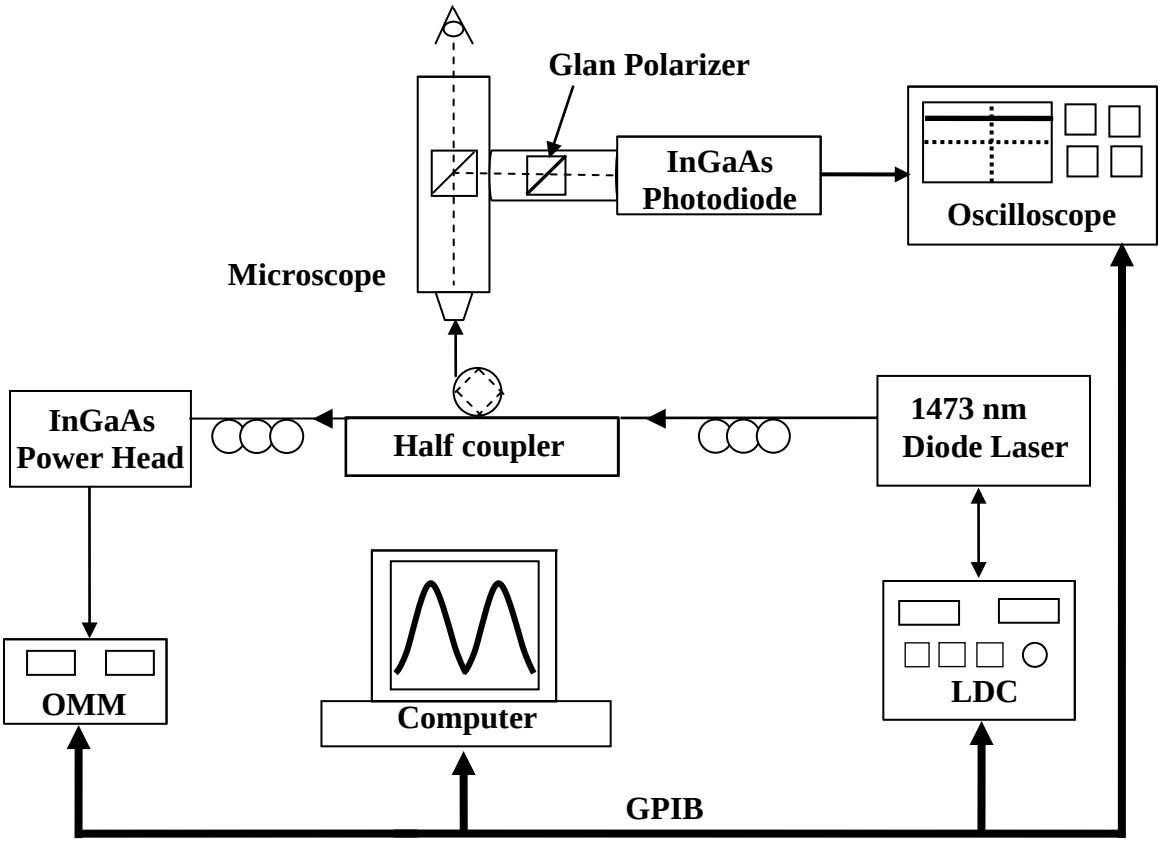

Figure 5.1(a): Schematic of the experimental setup

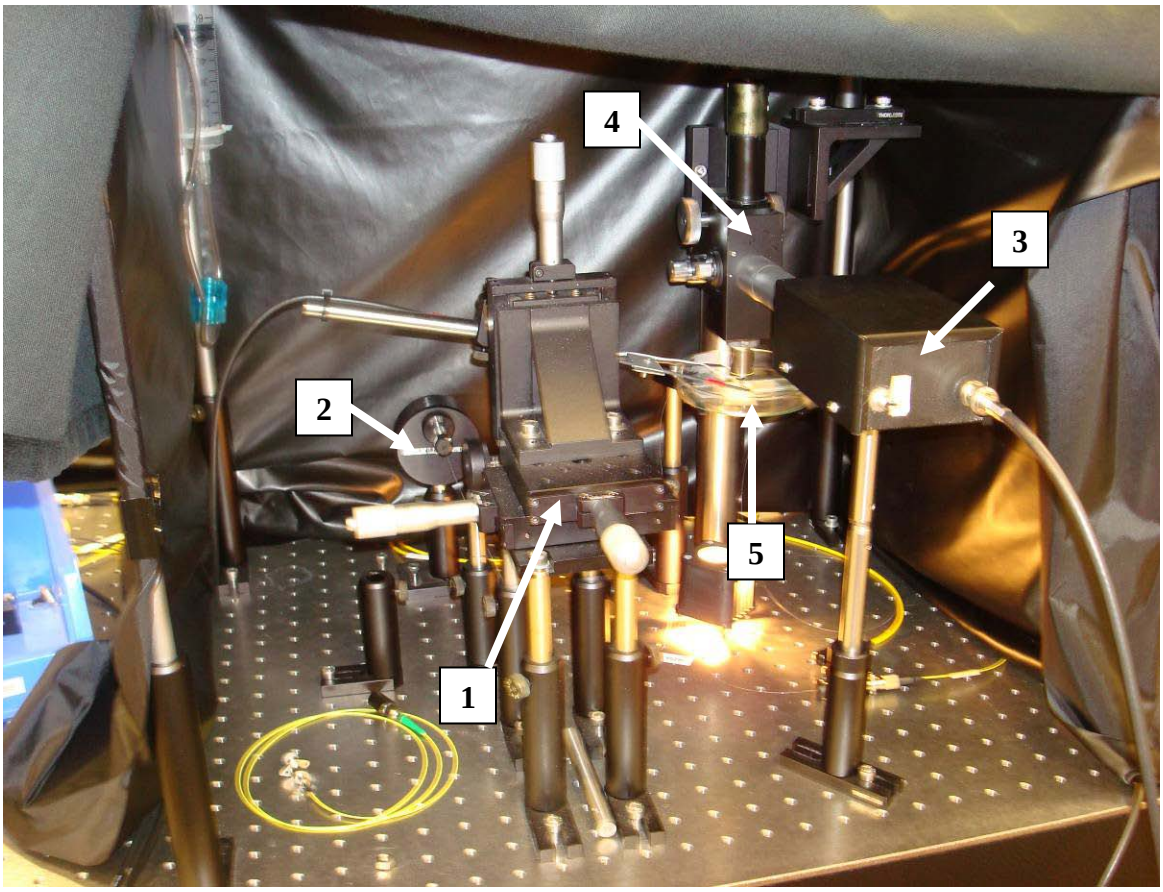

Figure 5.1(b): Experimental Setup

Device Number	Name
1	XYZ Translator
2	InGaAs Power Head Meter
3	InGaAs Photodetector
4	Microscope
5	Coupler Holder (See figure 5.1 (c))

Table 5.1: Experimental setup elements.

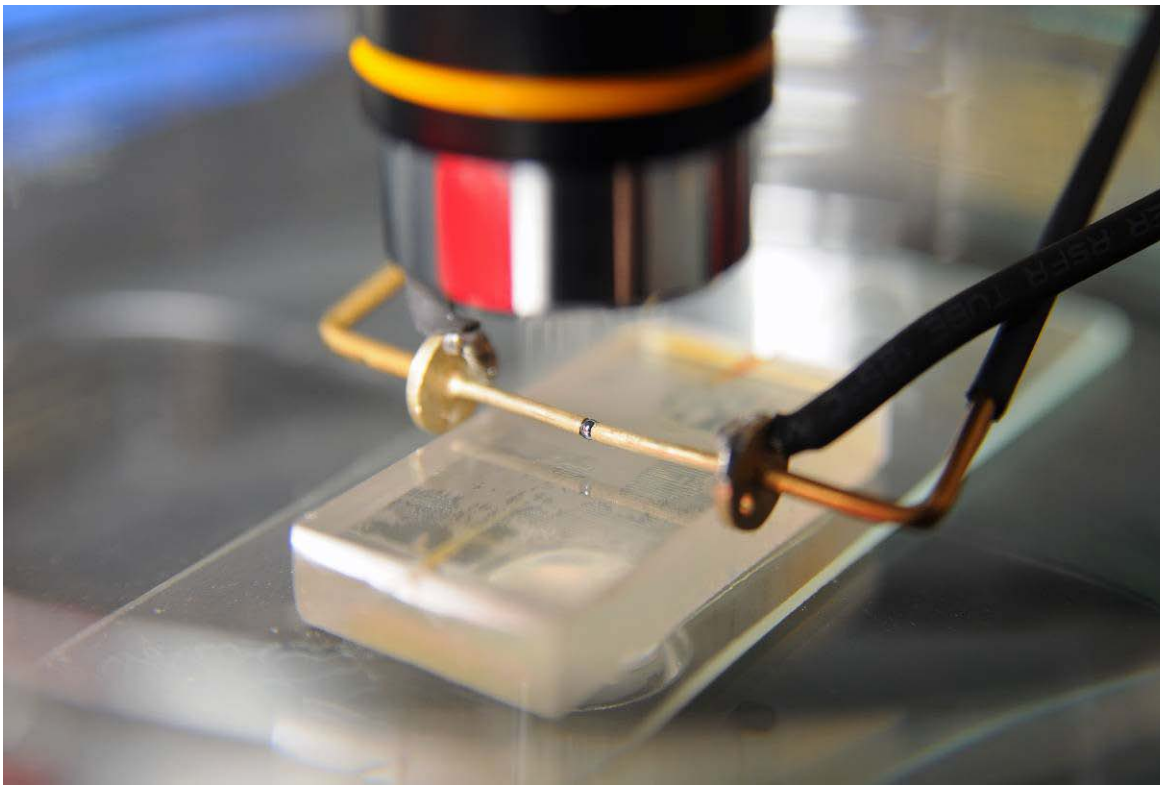

Figure 5.1 (c): Optical fiber coupler and a silicon sphere held between 2 golden probes.

5.3 Polarization Dependent Background in the Spectra

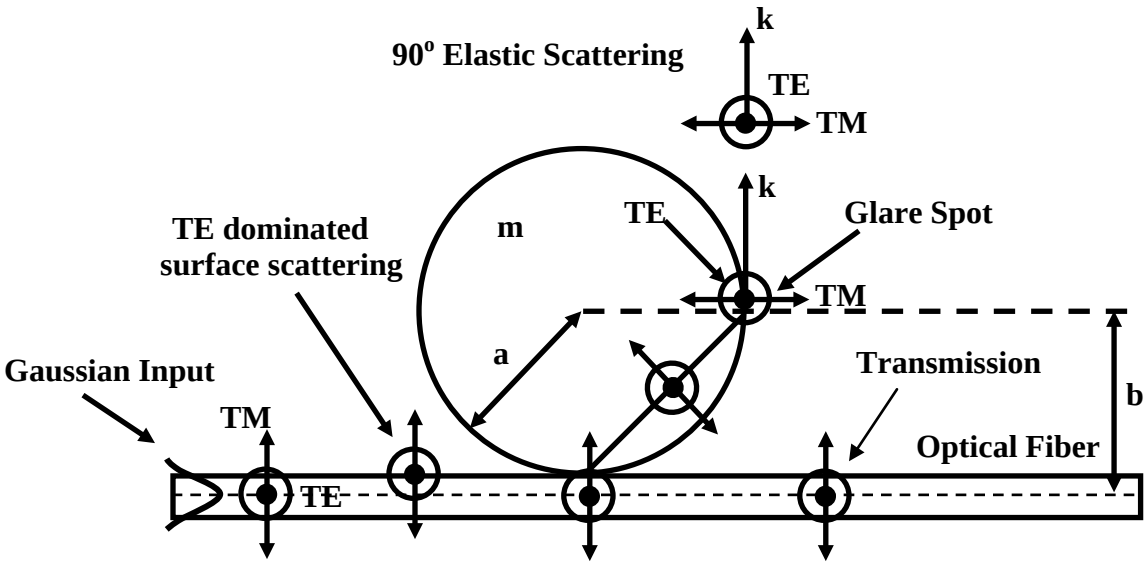

Figure 5.2 (a): Schematic illustration of a microsphere coupled to an optical fiber placed at an impact parameter b away from the sphere center.

Figure 5.2 (a) shows a microsphere of radius a and index of refraction m coupled to an optical fiber placed at an impact parameter b away from the sphere center. The transverse electric (TE) and transverse magnetic (TM) components with respect to the sphere of a Gaussian beam are shown in figure 5.2 (a) traveling in the optical fiber and inside the sphere. The TE component is pointing outside the paper, while the TM component is perpendicular to the fiber. As the electromagnetic wave couples to the sphere, the TM component refracts from the sphere parallel to the direction of the optical fiber. The background due to the scattering from the coupler's surface has more TE polarized component than TM polarized component. Moreover, the background from the glare spot

should be the same in the TE and TM polarized spectra. As a result, if the polarizer in figure 5.1 (a) is rotated to transmit the TM component, the scattering from the sphere at the glare spot will be detected only. Consequently, less background will be seen in the TM polarized spectra. On the other hand, if the polarizer in figure 5.1 (a) is rotated to transmit the TE component, the scattering of light from the coupler, as well as the sphere, and the glare spot will be detected. Consequently, more background (BG) will be present in the TE polarized spectra.

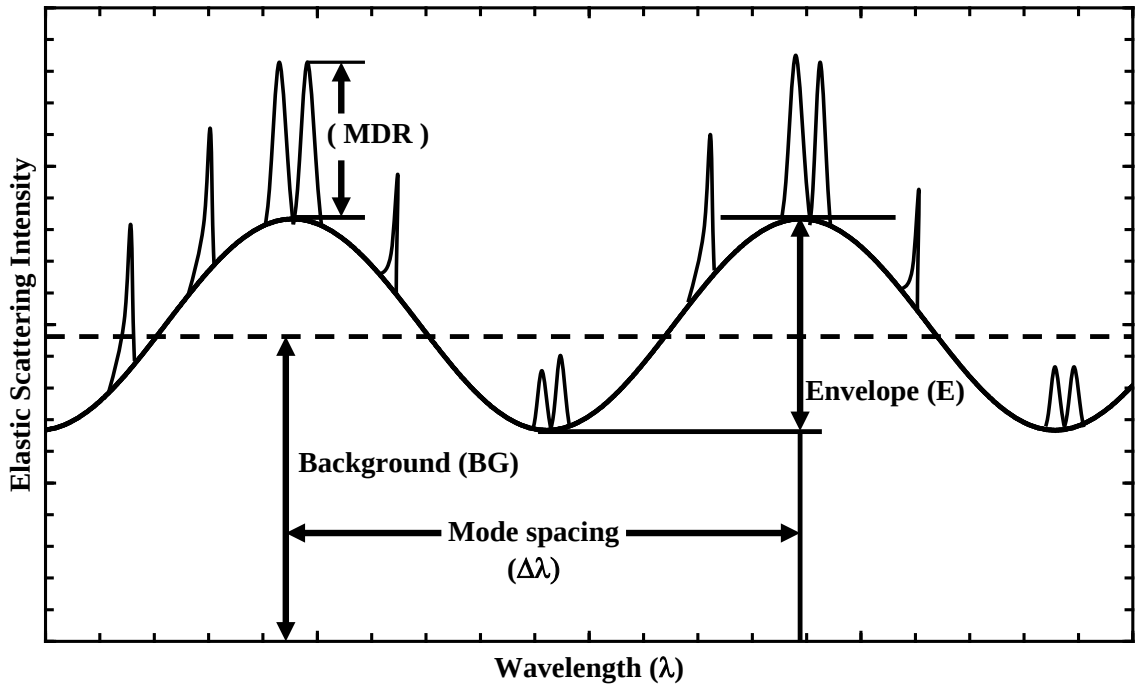

Figure 5.2 (b): Illustration of a spectrum with the MDR, envelope, and background.

Figure 5.2 (b) shows an illustration of a spectrum defining the MDR, envelope (E) and background (BG) intensities in an explanatory spectrum. The slowly varying envelope

oscillates at mode spacing ($\Delta\lambda$), which is the spacing between the MDRs of same same mode order (l) and consecutive mode number (n). The slowly varying envelope is caused by the interference of MDR's with the same polarization. The MDR's shape is same in the TE and TM polarized spectra. The background (BG) is the " dc " value of the spectrum. The MDR's have Lorenzian lineshapes on top of the envelope.

5.4 Explanation and Results

The calibration curve (wavelength versus temperature) of the 1473 nm diode laser used in the experiment is shown in figure 5.3. The wavelength of the laser varies with the temperature according to the equation

$$\lambda(\text{nm}) = 1467.1 + 0.3875T(^{o}\text{C}) \qquad (5.1),$$

where λ and T are the wavelength and temperature of the diode laser, respectively.

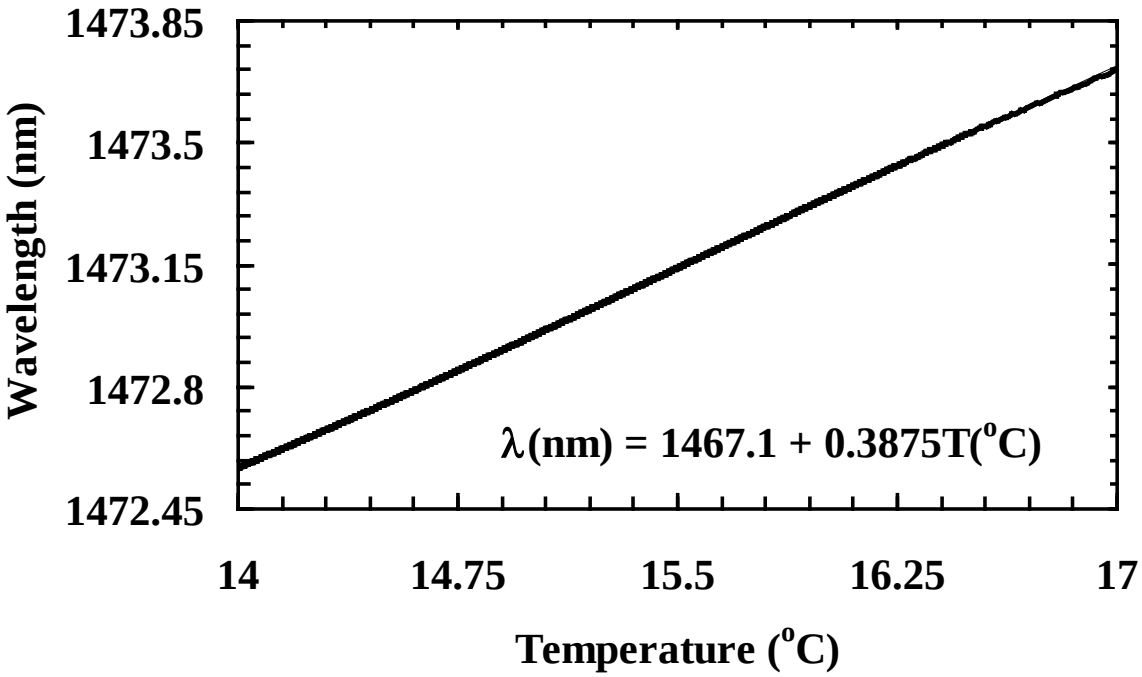

Figure 5.3: Laser wavelength as a function of temperature.

The microscope used to collect the scattering light from the sphere has two eyepieces. The scattered light is sent to the eyepieces by a beam splitter as shown in figure 5.1(a). The scattered light from the sphere at 90^o is reflected at an angle of 45^o before being detected by the InGaAs photodiode (PD). The resonances shown in figure 5.4(a), (b), and (c) are exhibited by the periodic circumnavigation of the electromagnetic wave inside the sphere. These resonances are size parameter ($x = 2\pi a/\lambda$) dependent and they are known as morphology dependent resonances (MDRs) [42].

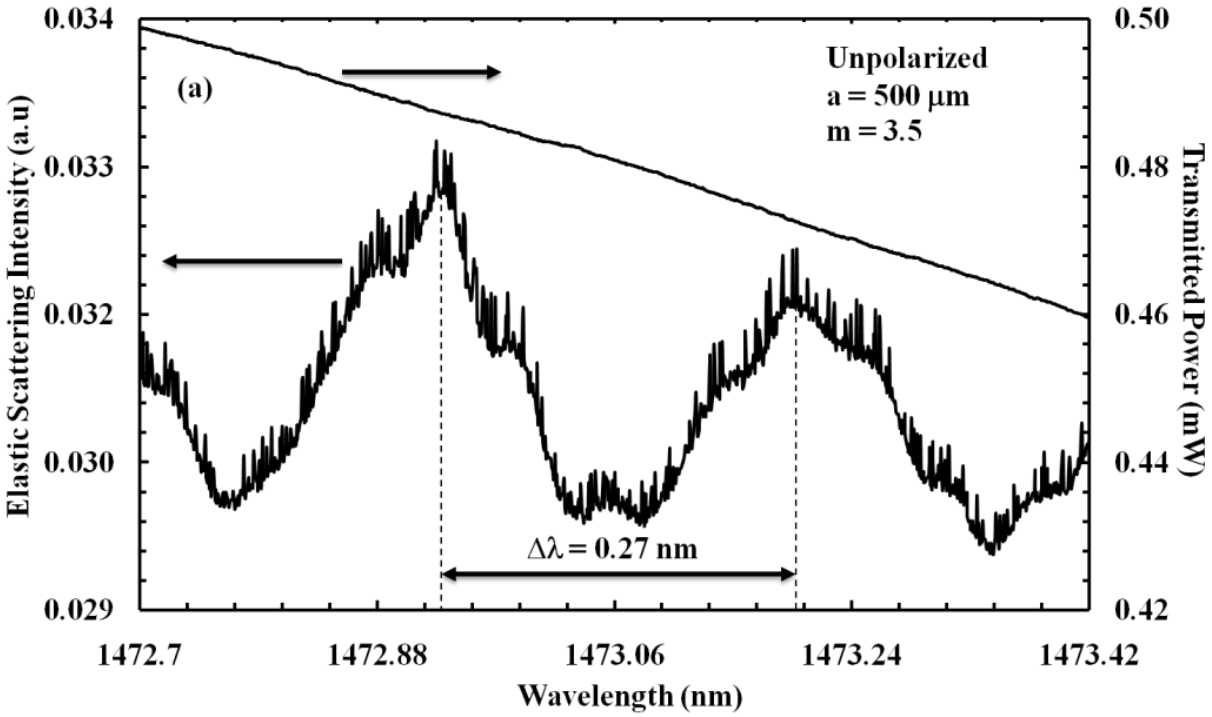

Figure 5.4 (a) High coverage spectra for the elastic scattering intensity without a polarizer.

Figure 5.4 (a) shows the high coverage spectrum of the elastically scattered light from the microsphere detected without a polarizer and the corresponding transmitted power. Figure 5.4 (b) and (c) present the spectra of the elastically scattered light from the silicon microsphere with a polarizer in the detection path as shown in Figure 5.1 (a). Figure 5.4 (b) and (c) show the TE and TM polarized elastically scattered light from the silicon microsphere and the corresponding transmitted power. The mode spacing between the MDR's of same mode order (l) and consecutive mode numbers (n) is observed to be 0.27 nm, which agrees well with the result of 0.26 nm estimated at 1473 nm.

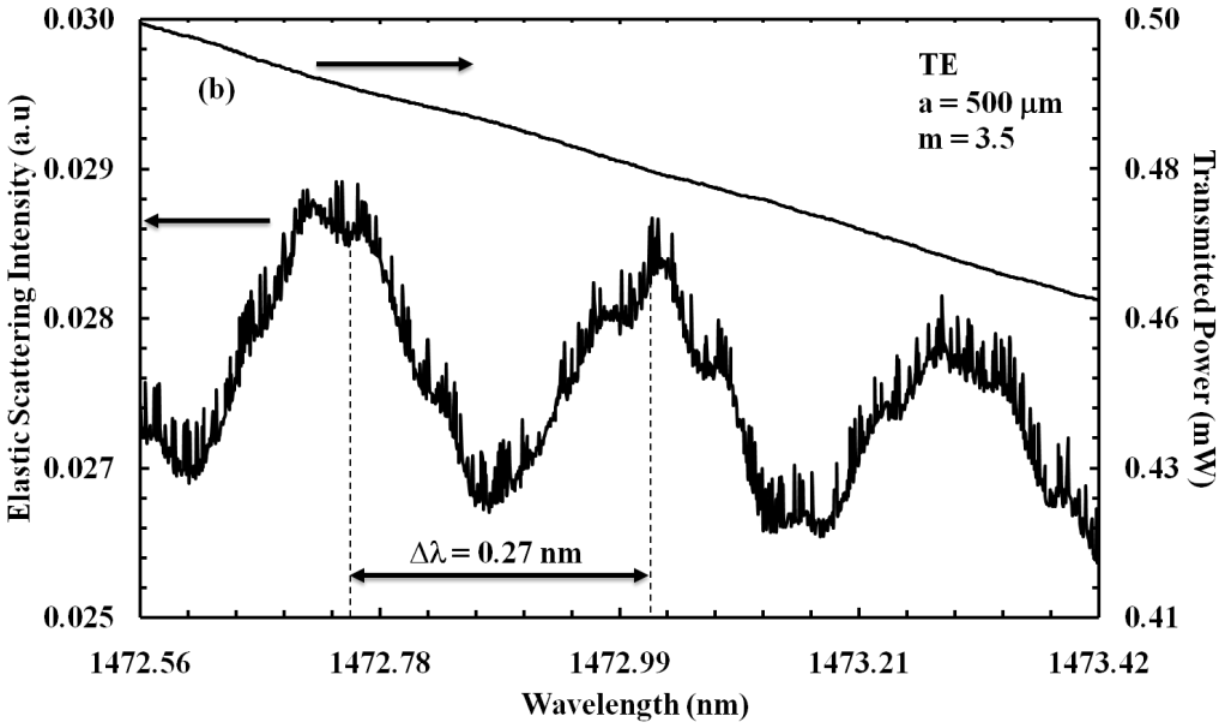

Figure 5.4(b) High coverage spectra for TE polarized elastic scattering intensity.

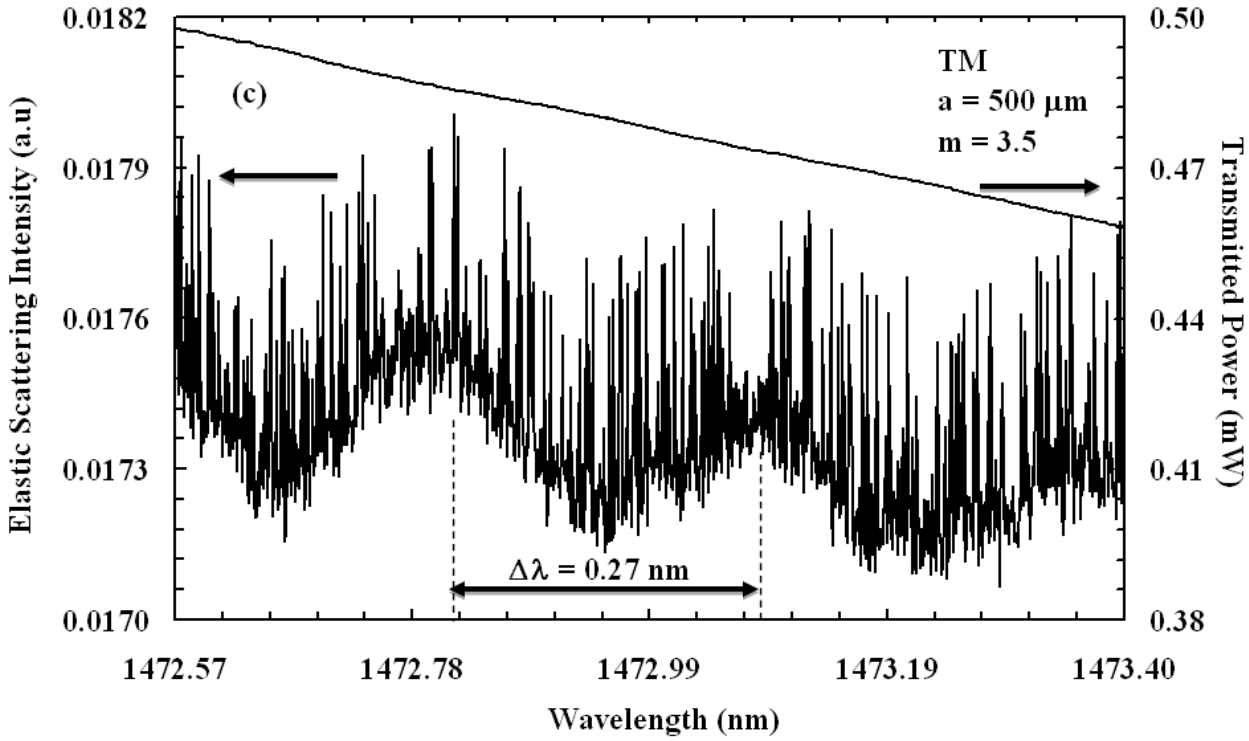

Figure 5.4(c) High coverage spectra for TM polarized elastic scattering intensity.

Using Eq. (3.16), the number of resonances was estimated to be approximately $4x10^4$. The observed number is approximately 400 in Figure 5.4 (a), (b), and (c). The mode order (l) ranges from 1 to x = 2130. As a result, 400 MDR's out of $4x10^4$ was observed, that is 200 mode orders out of the expected l = 2000 was seen. This means that the non observed resonances of order l = 1-1800 have sharper linewidths compared to the 0.0015 nm linewidth of the 1473 nm laser, and consequently higher quality factor (Q). Whereas, the observed 200 resonances have wider linewidths compared to the 0.0015 nm of the 1473 nm

laser, and consequently smaller quality factor than that of the 1473 nm laser, which was estimated to be 10^6.

The background in Figure 5.4 (a), (b), and (c) is due to the scattering from the half coupler surface as well as from the refracted beam (glare spot) [36]. The occurrence of closely located resonances in the TM polarized spectrum in Figure 5.4(c) is because of the large size of the silicon microsphere. The scattered intensity envelope in the TM polarized spectrum in Figure 5.4(c) has a smaller amplitude compared to that in the TE spectrum in Figure 5.4 (b) and in the spectrum without a polarizer in Figure 5.4 (a).

The unpolarized spectrum intensity ratio of MDR to envelope is 1:6. Whereas in the TE polarized spectra the ratio of MDR intensity to envelope is 1:4, and in the TM polarized spectra the ratio of MDR intensity to envelope is 2:1. Theoretically, the slowly varying envelope should be the same for the TE and TM polarized elastic scattering intensity [70]. The slowly varying envelopes in Figure 5.4 (b), and (c) are different as a result of the position dependent coupling of the light to the sphere, which would affect the TE and TM polarized scattering. Figure 5.4 (a) shows that there is more TE component than TM component in the unpolarized spectrum because of the position dependent coupling.

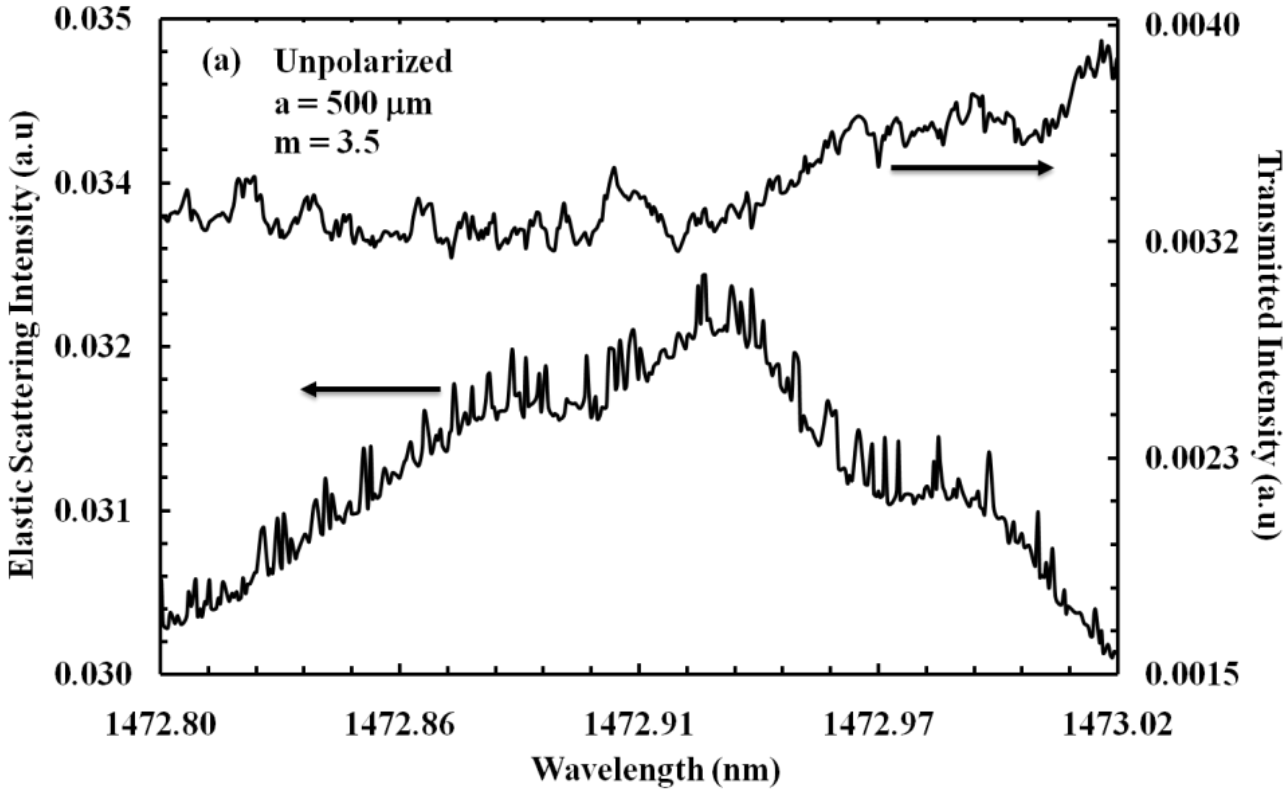

Figure 5.5 (a) High resolution spectra for the elastic scattering intensity without a polarizer.

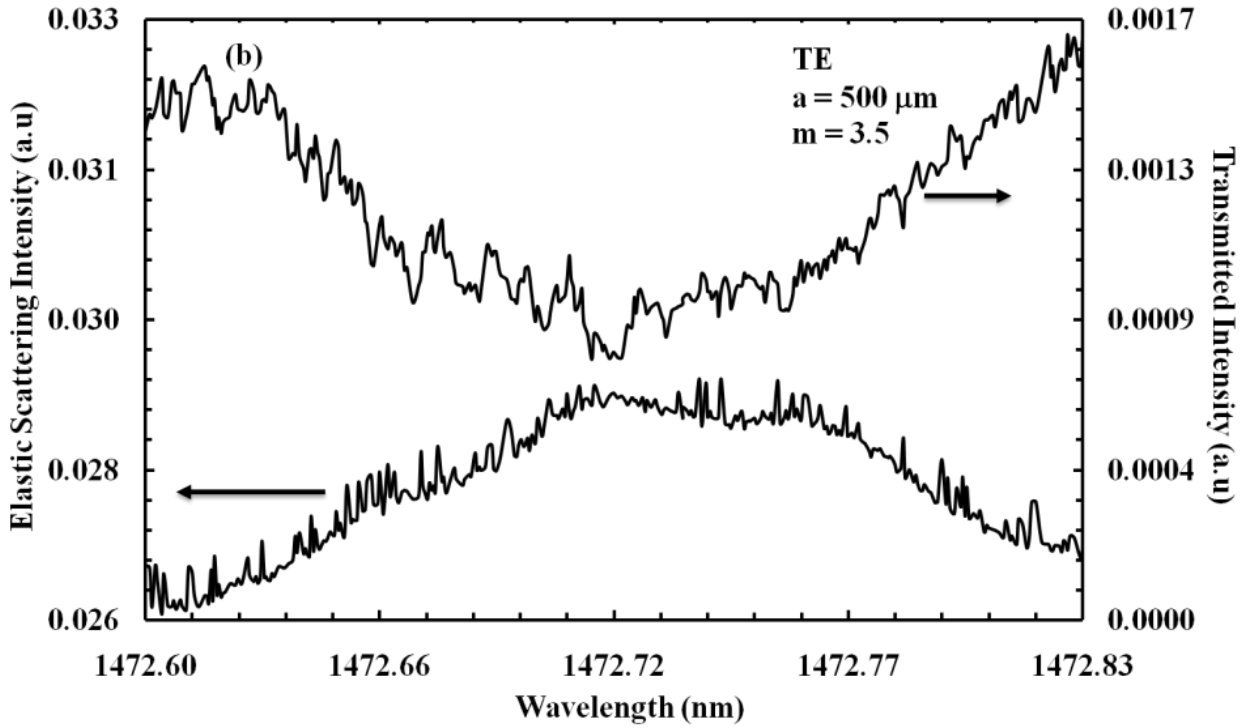

Figure 5.5 (b). High resolution spectra for TE polarized elastic scattering intensity.

The transmitted power spectrum was observed in figure 5.4 (a), and (b) to be almost a straight line and hard to distinguish between the dips. Consequently, in order to increase the resolution of the transmitted dips, a trendline was fitted to the transmitted power spectrum. Then the equation of the trendline was calculated as a function of the wavelength. The new values of the transmitted power were calculated according to the trendline equation and then subtracted from the original transmitted power values. A new curve for the transmitted power was fitted as shown in figure 5.5 (a), and (b). Figure 5.5 (a), and (b) show the high resolution spectra of figure 5.4 (a), and (b) respectively. As expected for every peak in the scattered spectra, there is a corresponding dip in the transmitted power spectra.

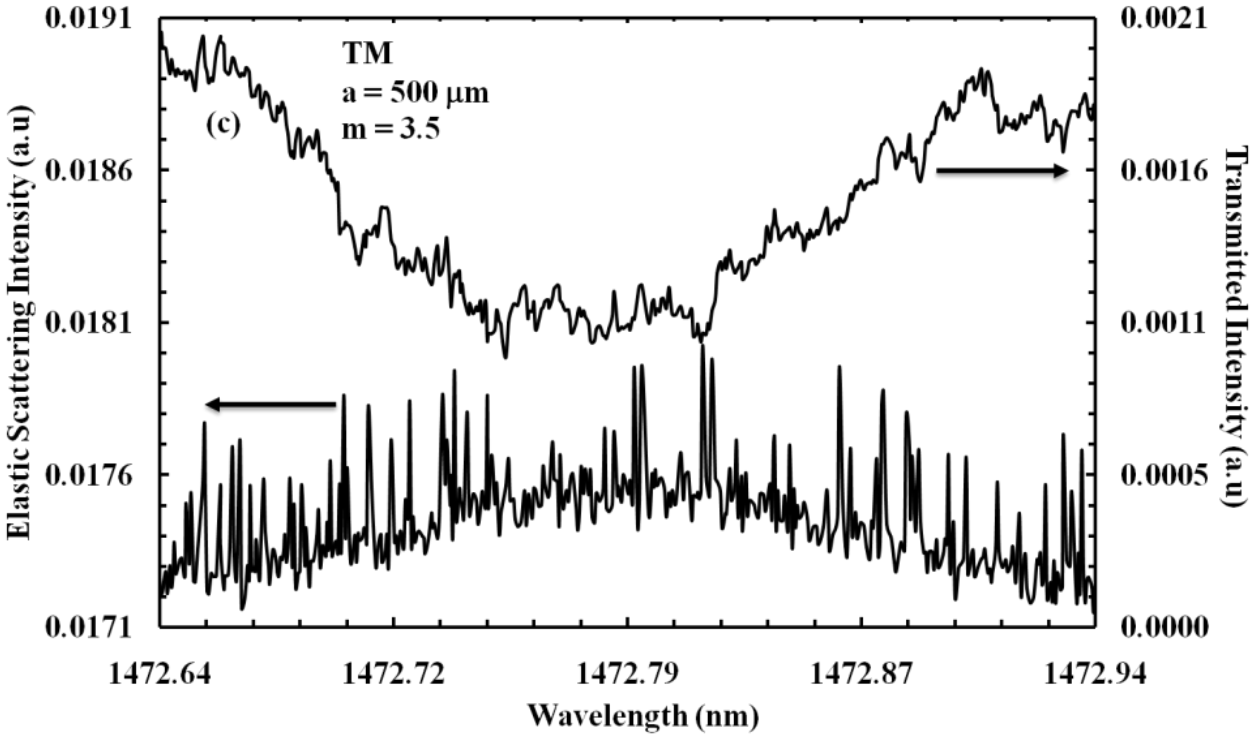

Figure 5.5 (c). High resolution spectra for TM polarized elastic scattering intensity.

The transmitted power spectrum was observed in figure 5.4(c) to be almost a straight line and hard to distinguish between the dips. Consequently, in order to increase the resolution of the transmitted dips, a trendline was fitted to the transmitted power spectrum. Then the equation of the trendline was calculated as a function of the wavelength. The new values of the transmitted power were calculated according to the trendline equation and then subtracted from the original transmitted power values. A new curve for the transmitted power was fitted as shown in figure 5.5(c). Figure 5.5(c) shows the high resolution spectra of figure 5.4(c). As expected for every peak in the scattered spectra, there is a corresponding dip in the transmitted power spectra.

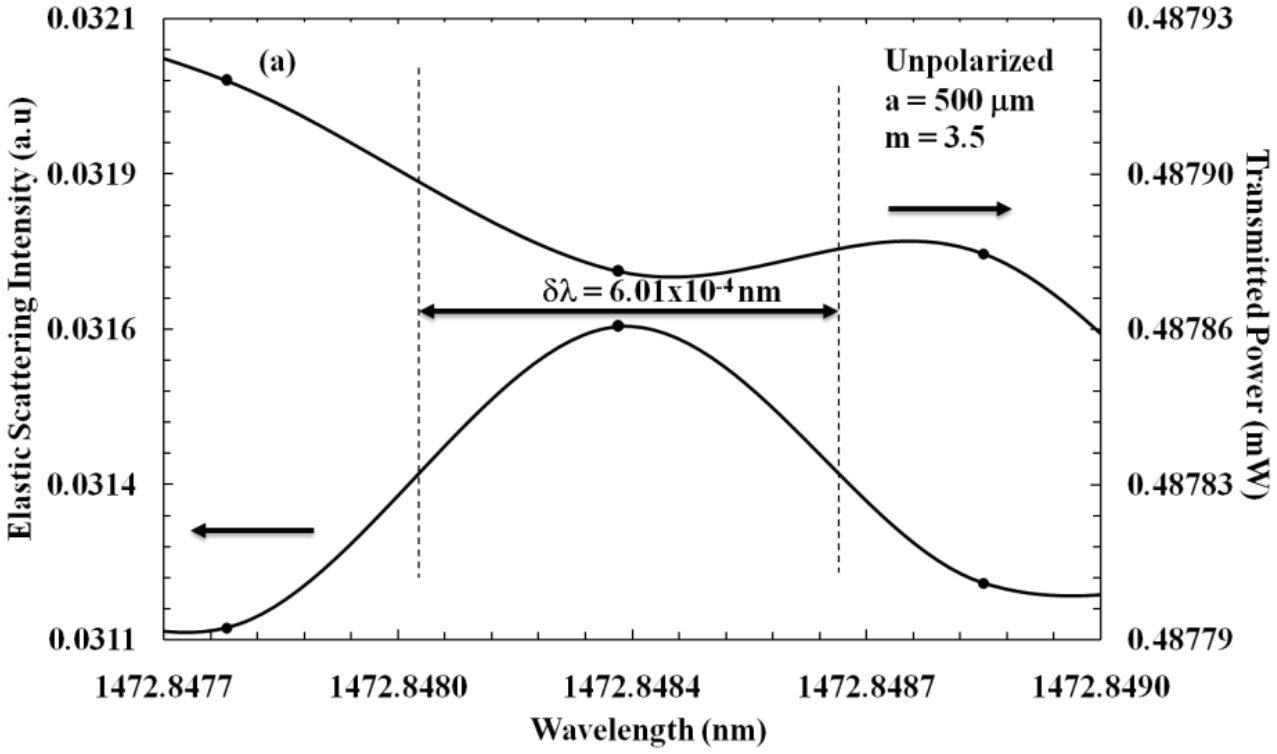

Figure 5.6 (a). Single resonance spectra of the elastic scattering intensity without a polarizer

Figure 5.6(a) shows the single resonance picked up from figure 5.4(a). The linewidth of the MDR is found to be of the order of 10^{-4} nm, which corresponds to a quality factor ($Q = \lambda/\delta\lambda$) of the order 10^{6}. At the MDRs of wavelength 1472.8484 nm of figure 5.6(a), the transmitted power drops by about 0.02 % of the incident power. The scattered intensity signal has a large dynamic range on the order of 18dB.

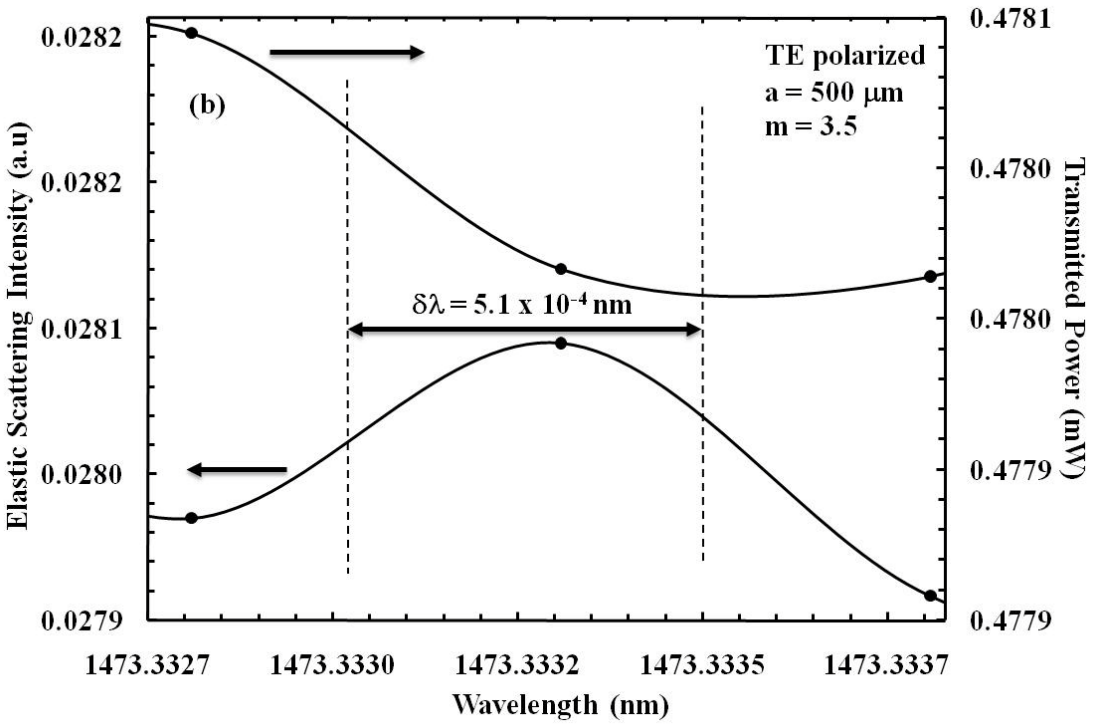

Figure 5.6 (b). Single resonance spectra for TE polarized elastic scattering intensity.

Figure 5.6(b) shows the single resonance picked up from figure 5.4(b). The linewidth of the MDR is found to be of the order of 10^{-4} nm, which corresponds to a quality factor ($Q =$

$\lambda/\delta\lambda$) of the order 10^6. At the MDRs of wavelength 1473.333 nm of figure 5.6(b), the transmitted power drops by about 0.02 % of the incident power. The scattered intensity signal has a large dynamic range on the order of 22dB.

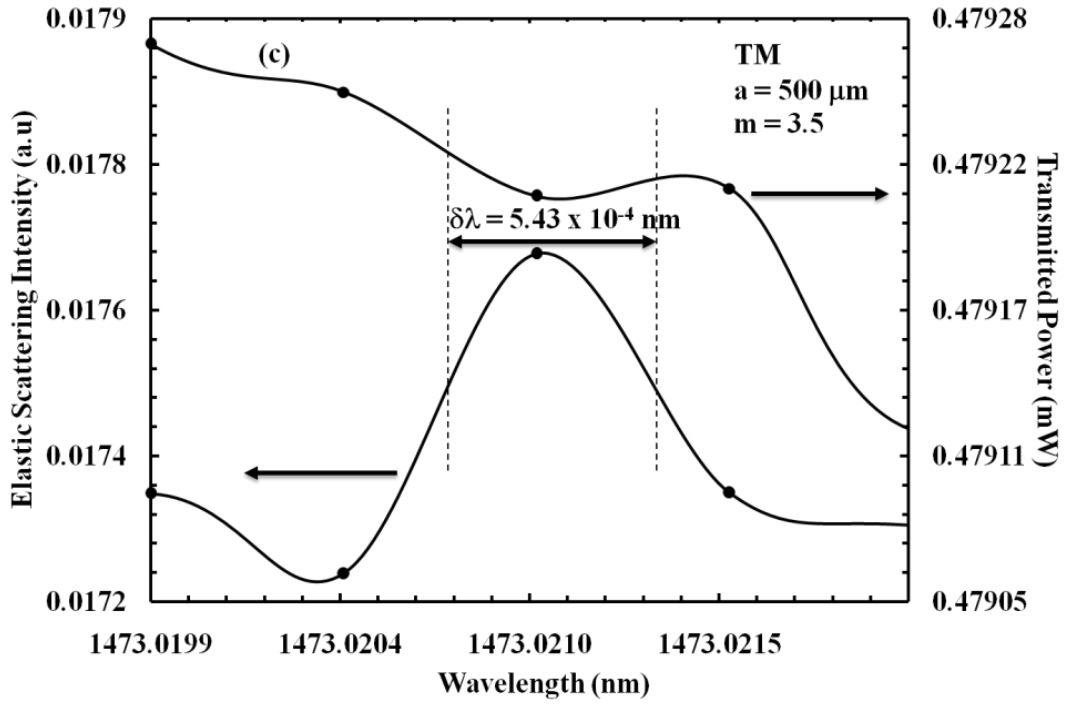

Figure 5.6 (c). Single resonance spectra for TM polarized elastic scattering intensity.

Figure 5.6(c) shows the single resonance picked up from figure 5.4(c). The linewidth of the MDR is found to be of the order of 10^{-4} nm, which corresponds to a quality factor (Q = $\lambda/\delta\lambda$) of the order 10^6. At the MDRs of wavelength 1473.0210 nm of figure 5.6(c), the transmitted power drops by about 0.02 % of the incident power. The scattered intensity signal has a large dynamic range on the order of 17dB.

6.1 Conclusions and Future Work

A brief description was given in this thesis about the elastic scattering from spherical particles, the morphology dependent resonances (MDRs), and their excitation principle using a Gaussian beam. The importance of silicon photonics, the latest achievements, the applications in the field, as well as the latest studies of promising applications that can be done using a silicon microsphere, were presented. Also, theoretical calculations for elastic light scattering from a 50 μm, 3.5 refractive index silicon microsphere were presented and analysed in the 1200 nm region. The mode spacing between MDRs with consecutive mode orders was observed to be 1.76 nm. The full width half maximum of MDRs was found to be 0.02 nm, which corresponds to a quality factor of 10^5. The transmission signal is not suitable for signal monitoring, but the 90^o elastic scattering has a larger dynamic range is suitable for crosstalk suppression between channels. The TE and TM polarized MDRs of the microsphere can be easily used separately with the use of a polarizer. The 90^o elastic scattering light can be accumulated using a high numerical aperture lens and measured using an InGaAs photodetector. The transmitted intensity can be measured using an optical multimeter. The photocurrent can be measured using a current meter in series with the sphere and voltage supply.

Experimental spectra for unpolarized, TE, and TM polarized elastic light scattering from a 500 μm radius and 3.48 refractive index silicon microsphere were presented and analysed between 1472-1473 nm. The TE and TM MDR's of the microsphere here can also be detected separately with the use of a polarizer. The mode spacing was observed to be 0.27 nm, which correlates well with the optical size of the silicon microsphere. The full-width-half-maximum of the MDRs were found on the order 10^{-4} nm, which correspond to a quality factor of 10^6. The transmission signal is not suitable for signal monitoring, while the 90^o elastic scattering with a larger dynamic range, is suitable for applications such as channel dropping. The polarization dependence of the elastic scattering signal heralds another novel parameter from optical channel dropping.

For the silicon microsphere of radius 500 μm to be used as an RCE photodetector, a laser of wavelength range 1.07-1.19 μm is needed. This corresponds to the low absorption coefficient needed, in order for the electromagnetic wave to be able to resonate inside the sphere and at the same the photons having enough energy to cross the band gap from the valence up to the conduction band. It is important to note that, if we have silicon spheres ωιτη α radius smaller than 500 μm, then it is possible to have an RCE photodetector at a wavelength around 1100 nm.

BIBLIOGRAPHY

[1] H. C. van de Hulst, "Light Scattering by Small Particles," Dover Publications, New York, 1981.

[2] S. C. Hill and P. W. Barber, "Light Scattering by Particles: Computational Methods," World Scientific, Singapore, 1990.

[3] H. Rong, R. Jones, A. Liu, O. Cohen, D. Hak, A. Fang, and M. Paniccia, "A Continuous-Wave Raman Silicon Laser," Nature, vol. 433, pp. 725-728, 2005.

[4] O. Boyraz, and B. Jalali, "Demonstration of directly modulated silicon Raman laser", *Opt. Exp.* vol.13, pp. 796-800, 2005.

[5] R. Jones et al., "Lossless Optical Modulation in a Silicon Waveguide using Stimulated Raman Scattering," Opt. Exp., vol. 13, pp. 1716-1723, 2005.

[6] R. Soref, and J. Lorenzo, "All-Silicon Active and Passive guided-Wave Components for λ = 1.3 and 1.6 μm," IEEE J. Quantum Electron., Vol. QE-22, pp. 873-879, 1986.

[7] R. A. Soref, and B. R. Bennett, "Kramers-Kronig Analysis of E-O Switching in Silicon," Proc. SPIE Integr. Opt. Circuit Eng., Vol. 704, pp. 32-37, 1986.

[8] B. Schuppert, J. Schmidtchen, and K. Petermann, "Optical Channel Waveguides in Silicon Diffused from GeSi Alloy," Electron. Lett., Vol. 25, pp. 1500-1502, 1989.

[9] R. A. Soref, J. Schmidtchen, and K. Petermann, "Large Single-Mode Rib Waveguides in GeSi and Si-on-SiO2," IEEE J. Quantum Electron, Vol. 27, pp. 1971-1974, 1991.

[10] P. D. Trinh, S. Yegnanarayanan, and B. Jalali, "Integrated Optical Directional Couplers in Silicon-on-Insulator," Electron. Lett., Vol. 31, pp. 2097-2098, 1995.

[11] U. Fischer, T. Zinke, and K. Petermann, "Integrated Optical Waveguide Switches in SOI," Proc. IEEE Int. SOI Conf., pp. 141-142, 1995.

[12] T. T. H. Eng, S. S. Y. Sin, S. C. Kan, and G. K. L. Wong, "Surface Micromachined Movable SOI Optical Waveguides," Proc. Int. Conf. Solid-State Sens. Actuators, Vol. 1, pp. 348-350, 1995.

[13] C. Z. Zhao, G. Z. Li, E. K. Liu, Y. Gao, and X. D. Liu, "Silicon on Insulator Mach-Zehnder Waveguide Interferometers Operating at 1.3 μm," Appl. Phys. Lett., Vol. 67, pp. 2448-2449, 1995.

[14] P. D. Trinh, S. Yegnanarayanan, and B. Jalali, "5 x 9 Integrated Optical Star Coupler in Silicon-on-Insulator technology," IEEE Photon. Technol. Lett., Vol. 8, pp. 794-796, 1996.

[15] P. D. Trinh, S. Yegnanarayanan, F. Coppinger, and B. Jalali, "Silicon on-Insulator (SOI) Phased-Array Wavelength Multi-Demultiplexer with Extremely Low-Polarization Sensitivity," IEEE Photon. Technol. Lett., Vol. 9, pp. 940-942, 1997.

[16] B. Jalali, S. Yegnanarayanan, T. Yoon, T. Yoshimoto, I. Rendina, and F. Coppinger, "Advances in Silicon-on-Insulator Optoelectronics," IEEE J. Sel. Topics Quantum Electron., Vol. 4, pp. 938-947, 1998.

[17] J. D. Plummer, M. D. Deal, and P. B. Griffi, " Silicon VLSI Technology," Upper Saddle River, Prentice-Hall, New Jersey, 2000.

[18] B. Jalali, and S. Fathpour, "Silicon Photonics," IEEE Journal of Lightwave Technology, Vol. 24, pp. 4600-4615, 2006.

[19] C. Gunn, "CMOS Photonics for High Speed Interconnects," IEEE Micro, Vol. 26, pp. 58-66, 2006.

[20] D. A. B. Miller, "Optical Interconnects to Silicon," IEEE J. Sel. Topics Quantum Electron., Vol. 6, pp. 1312-1317, 2000.

[21] K. J. Vahala, ed. "Optical Microcavities," World Scientific, Singapore, 2004.

[22] E. Özbay, M. S. Islam, B. Onat, M. Gökkavas, O. Aytür, G. Tuttle, E. Towe, R. H. Henderson, and M. S. Ünlü, "Fabrication of High speed Resonant Cavity Enhanced Schottky Photodiodes," IEEE Photon. Technol. Lett., Vol. 9, pp. 672-674, 1997.

[23] T. Knödl, H. K. Choy, J. L. Pan, R. King, R. Jager, G. Lullo, J. F. Ahadian, R. J. Ram, C. G. Fonstad, and K. J. Ebeling, "RCE Photodetectors Based on VCSEL Structures," IEEE Photon. Technol. Lett., Vol. 11, pp. 1289-1291, 1999.

[24] B. Butun, N. Biyikli, I. Kimukin, O. Aytur, P. A. Postigo, J. P. Silveira, and A. R. Alija, "High Speed 1.55 μm Operation of Low-Temperature-Grown GaAs-Based Resonant Cavity Enhanced p-i-n Photodiodes," Appl. Phys. Lett., Vol. 84, pp. 4185-4187, 2004.

[25] M. S. Ünlü, M. K. Emsley, O. I. Dosunmu, P. Muller, and Y. Leblebici, "High Speed Si Resonant Cavity Enhanced Photodetectors and Arrays," Vac. Sci. Technol., Vol. 22, pp. 781-787, 2004.

[26] N. E. J. Hunt, E. F. Schubert, and G. J. Zydzik, "Resonant Cavity p-i-n Photodetector Utilizing an Electron Beam Evaporated Si/SiO2 Microcavity," Appl. Phys. Lett., Vol. 63, pp. 391-393, 1993.

[27] Z. Djuric, P. Krstajic, M. Smiljanic, and D. Randjelovic, "The Effect of Diffusion on the Impulse Response of RCE Detector," IEEE Photon. Technol. Lett., Vol. 13, pp. 620-622, 2001.

[28] L. Pavesi, "Will Silicon be the Photonics Material of the Third Millennium?" J. Phys. Condens. Matter, Vol. 15, pp. 1169-1196, 2003.

[29] I. S. Grudinin, V. S. Ilchenko, and L. Maleki, "Ultrahigh optical Q factors of Crystalline Resonators in the Linear Regime," Phys. Rev. A, vol. 74, pp. 63806-63815, 2006.

[30] H. Zimmermann, "Integrated Silicon Optoelectronics," Springer Verlag, Berlin, 2000.

[31] M. Gharghi, H. Bai, G. Stevens, and S. Sivoththaman, "Three-Dimensional Modeling and Simulation of p-n Junction Spherical Silicon Solar Cells," IEEE Transactions On Electron Devices, Vol. 53, pp. 1355-1363, 2006.

[32] A. Serpengüzel, and A. Demir, "Silicon Microspheres for near-IR communication applications," Semicond. Sci. Technol., Vol. 23, pp. 64009-64017, 2008.

[33] A. Serpengüzel, A. Kurt, and U. K. Ayaz, "Silicon Microspheres for electronic and Photonic Integration," Photonics and Nanostructures - Fundamentals and Applications, Vol. 6, pp. 179-182, 2008.

[34] R. Hull, ed. “Properties of Crystalline Silicon,” IET, London, 1999.

[35] P.W. Barber, and R. K. Chang, ed. "Optical Effects Associated With Small Particles," World Scientific, Singapore, 1988.

[36] A. Serpengüzel, S. Arnold, G. Griffel, and J. A. Lock, “Enhanced Coupling to Microsphere Resonances with Optical Fibers,” J. Opt. Soc. Am. B, vol. 14, pp. 790-795, 1997.

[37] E. M. Purcell, “Spontaneous Emission Probabilities at Radio Frequencies,” Phys. Rev., vol. 69, pp. 681, (1946).

[38] S. C. Ching, H. M. Lai, and K. Young, "Dielectric microspheres as optical cavities: thermal spectrum and density of states," J. Opt. Soc. Am. B **4**, pp. 1995, 1987.

[39] S. C. Ching, H. M. Lai, and K. Young, "Dielectric microspheres as optical cavities: Einstein *A* and *B* coefficients and level shift," J. Opt. Soc. Am. B **4**, pp. 2004, 1987.

[40] S. K. Kim, A. L. Huston, and A. J. Campillo, "Optical Scattering as a Probe of local Field Effect in Micron-sized CdS Spheres," Bull. Korean. Chem. Soc., Vol. 16, pp. 96-101, 1995

[41] G. Kozyreff, J. L. Dominguez, and J. Martorell, "Whispering Gallery Mode Phase Matching for Surface Second Order Nonlinear Optical Processes in SPeherical Microresonators," Phys. Rev. A, Vol. 77, pp. 43817- 43826, 2008.

[42] B. R. Johnson, "Theory of Morphology Dependent Resonances: Shape Resonances and Width Formulas," J. Opt. Soc. Am. A, Vol. 10, 1993.

[43] P. R. Cornell, P. W. Barber, and C. K. Rushforth, "Resonant Spectra of dielectric Spheres," J. Opt. Soc. Am. A, Vol. 1, pp. 62-66, 1984.

[44] D. S. Benincasa, P. W. Barber, J.-Z. Zhang, W.-F. Hsieh, and R. K. Chang, "Spatial distribution of the internal and near-field intensities of large cylindrical and spherical scatterers," Appl. Opt. **26**, pp. 1348, 1987.

[45] E. E. M. Khaled, S. C. Hill, and P. W. Barber, ‘‘Internal electric energy in a spherical particle illuminated with a plane wave or off-axis Gaussian beam,’’ Appl. Opt. **33**, pp. 524, 1994.

[46] J.-Z. Zhang, D. H. Leach, and R. K. Chang, "Photon lifetime within a droplet: temporal determination of elastic and stimulated Raman scattering," Opt. Lett. **13**, pp. 270, 1988.

[47] J. P. Barton, D. R. Alexander, and S. A. Schaub, "Internal and near-surface electromagnetic fields for a spherical particle irradiated by a focused laser beam," J. Appl. Phys. **64**, pp. 1632, 1988.

[48] K. M. Lee, P. T. Leung, and K. M. King, "Dyadic Formulation of Morphology-Dependent Resonances," J. Opt. Soc. Am. B, Vol. 16, pp. 1406-1417, 1999.

[49] K. A. Fuller, "Scattering and Absorption Cross Sections of Compounded Spheres. II. Calculations for External Aggregation," J. Opt. Soc. Am. A, Vol. 12, pp. 881-892, 1995.

[50] G. Gouesbet, B. Maheu, and G. Grehan, "Light Scattering From a Sphere Arbitrarily Located in a Gaussian Beam, Using a Bromwich Formulation," J. Opt. Soc. Am. A, Vol. 5, pp. 1427-1443, 1988.

[51] C. A. Balanis, "Advanced Engineering electromagnetics," John Wiley and Sons, New York, 1989.

[52] J. A. Stratton, "Electromagnetic Theory," McGraw-Hill, New York, 1941.

[53] R. E. Collin, "The Field Theory of Guided Waves," IEEE press, New York, 1991.

[54] C. A. Balanis, "Advanced Engineering Electromagnetics," John Wiley and Sons, New York, 1989.

[55] B. R. Johnson, "Theory of Morphology Dependent Resonances: Shape Resonances With Width Fromulas," J. Opt. Soc. Am. A, Vol. 10, pp. 343-352, 1993.

[56] S. Arnold, "Microspheres, Photonics Atoms and the Physics of Nothing," American Scientist, Vol. 89, pp. 414-421, 2001.

[57] L. G. Guimardes, and H. M. Nussenzveig, "Theory of Mie Resonances and Ripple Fluctuations," Opt. Commun., Vol. 89, pp. 363-369, 1992.

[58] G. Roll, and G. Schweiger, "Geometrical Optic Model of Mie Resonances," J. Opt. Soc. Am. A, Vol. 17, pp. 1301-1311, 2000.

[59] T. J. A. Kippenberg, "Nonlinear Optics in Ultra High Q Whispering Gallery Optical Microcavities," Doctoral Dissertation, California Institute of Technology, California, 2004.

[60] G. Roll, and G. Schweiger, “Geometrical Optics Model of Mie Resonances,” J. Opt. Soc. Am. A., vol. 17, pp. 1301-1311, 2000.

[61] W. V. Klitzing, R. Long, V. S. Ilchenko, J. Hare, and V. Lefevre-Seguin, “Tunable Whispering Gallery Modes for Spectroscopy and CQED Experiments,” New Journal of Physics, 3, 14.1-14.14, 2001.

[62] J. A. Lock, and G. Gouesbet, “Generalized Lorenz-Mie Theory and Applications,” Journal of Quantitative Spectroscopy & Radiative Transfer, 110, pp. 800-807, 2009.

[63] C. F. Bohren and D. R. Huffman, Absorption and Scattering of Light by Small Particles, Interscience, New York, 1983.

[64] I. Gurvich, N. Shiloah, and M. Kleiman, “Calculations of The Mie Scattering Coefficients for Multilayered Particles with Large Size Parameters”, Journal of Quantitative Spectroscopy & Radiative Transfer, 70, pp. 433-440, 2001.

[65] M. L. Gorodetsky, A. A. Savchenkov, and V. S. Ilchenko, "Ultimate Q of Optical Microsphere Resonators," Opt. Letters, Vol. 21, pp. 453-455, 1996.

[66] S. Schiller, and R. L. Byer, "High Resolution Spectroscopy of Whispering Gallery Modes in Large Dielectric Spheres," Opt. Letters, Vol. 16, pp. 1138-1140, 1991.

[67] A. J. Campillo R. K. Chang [ed.]," optical Processes in Microcavities," Singapore : World Scientific, 1996.

[68] J. A. Lock, "An Improved Gaussian Beam Scattering Algorithm," Appl. Opt., Vol. 34, pp. 559-570, 1995.

[69] Q. Xu, B. Schmidt, J. Shakya, and M. Lipson, "Cascaded Silicon Microring Modulators for WDM Optical Interconnection," Opt. Express, Vol. 20, pp. 9430-9435, 2006.

[70] W. T. Grandy, “ Scattering of Waves from Large Spheres, ” Cambridge University Press, Cambridge, 2000.

APPENDIX

A.1 Electrical Control Input

A box for holding and operating a 1300 nm AT&T dual inline package (DIP) diode laser was prepared. The figures below show electrical connections of the laser to the laser diode controller, and the mechanical assembly steps of the laser box.

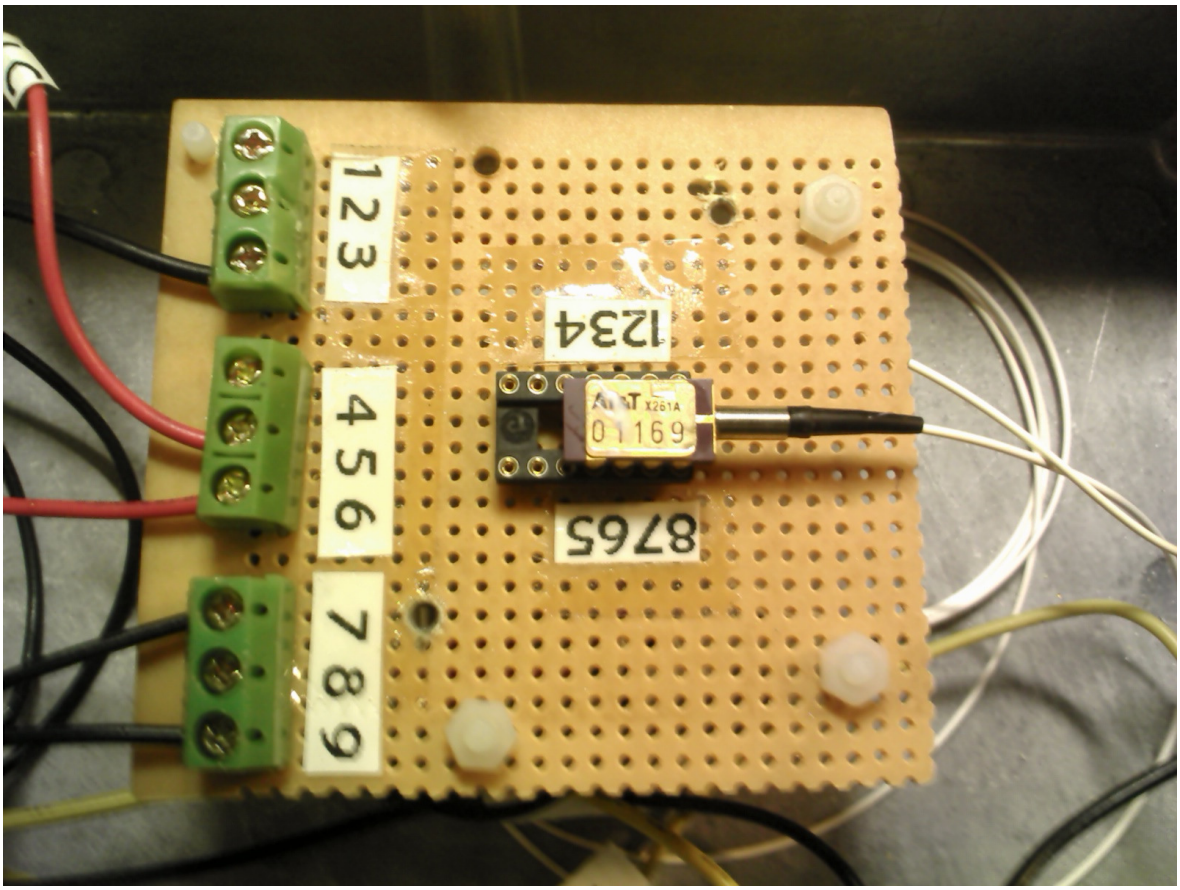

Figure A.1.1: Pigtailed diode laser in DIP package inserted in DIP socket.

Figure A.1.1 shows the Pigtailed diode laser in DIP package inserted in DIP socket. The labeled numbers around the socket corresponds to the numbers of the laser package pins. The green connectors are used to connect the socket pins to the laser diode current controller. The pins of the current connectors are numbered according to their connection with the laser diode current controller connectors. The connections between the laser package pins and the green connectors were done at the bottom side of the board.

Pin Number	**Pin Name**
1	Ground
2	Laser Anode
3	Laser Cathode
4	Ground
5	Ground
6	Photodiode Anode
7	Photodiode Cathode
8	Not Connected

Table A.1.1: Laser diode package pin numbers and their corresponding names.

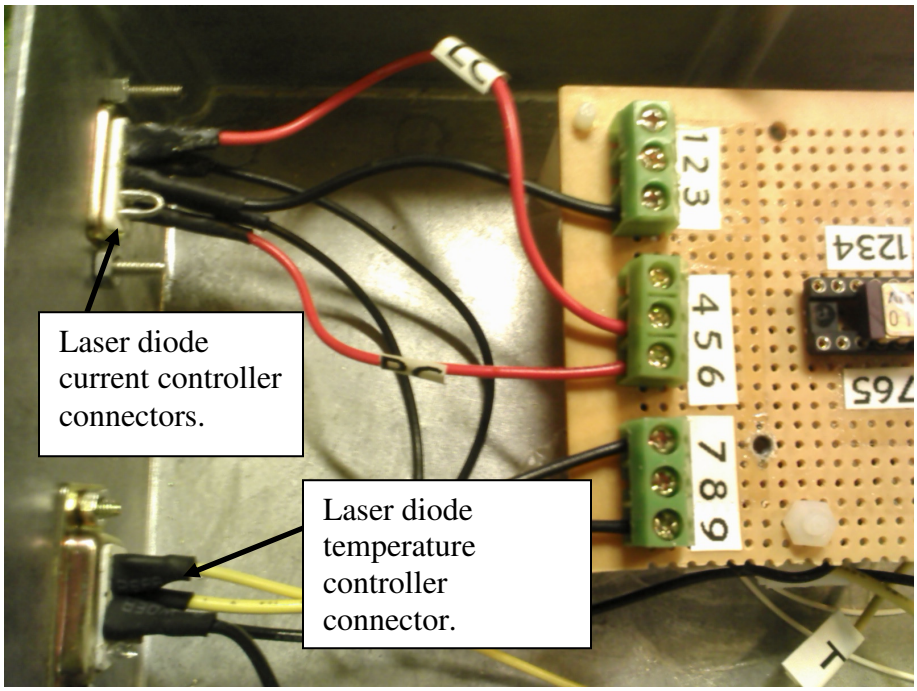

Figure A.1.2: Electrical connection to the laser diode current and temperature controller connectors.

Figure A.1.2 shows the electrical wiring connections of the green connectors to the laser diode current controller connector. The connections between the green connectors and the laser chip electrodes were done according to the table below.

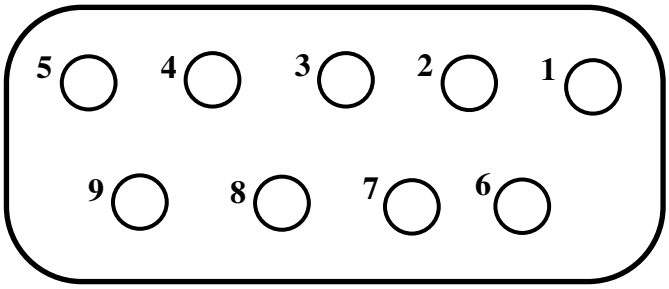

Figure A.1.3: Laser diode current controller back connector.

Pin Number	Pin Name
1 and 2	Free ends
3	Ground
4 and 5	Laser Cathode
6	Photodiode Cathode
7	Photodiode Anode
8 and 9	Laser Anode

Table A.1.2: Laser diode current controller connector numbers and their corresponding names.

A.2 Fiber Optic Output

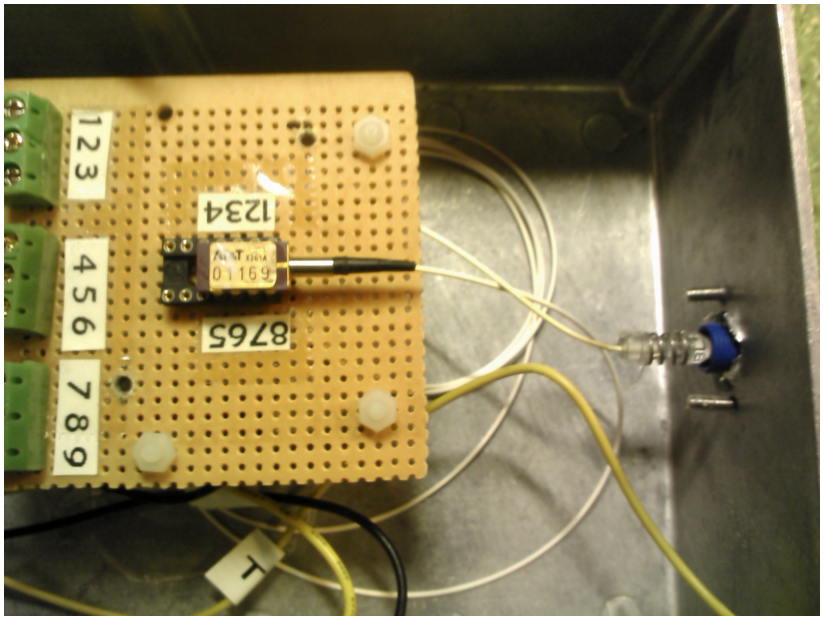

Figure A.2.1: Laser output fiber connected to a fiber adapter at the output of the box.

Figure A.2.1 shows the laser output fiber connected to an FC/PC fiber adapter at the output of the box.

A.3 Thermal Control Input

After the electrical connection, we need to connect the thermistor to the laser which would the information about the laser chip temperature.

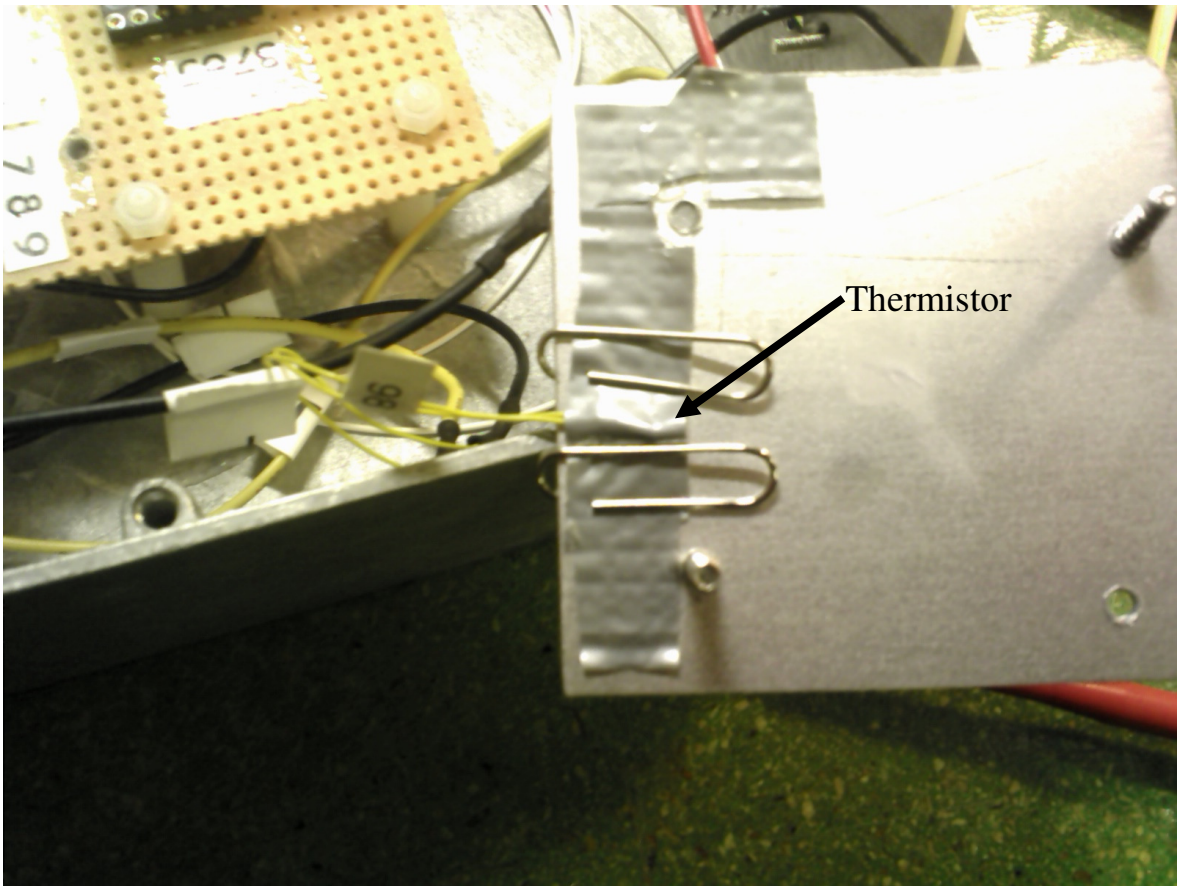

Figure A.3.1: Thermistor laying on a thin aluminum plate.

Figure A.3.1 shows the thermistor of part number 1T1002-5 laying on a thin aluminum plate. The thermistor was tied down to the aluminum sheet by a duct tape, and supported

with two metallic staples. The thermistor's positive and negative electrodes are connected to the laser diode temperature controller pins 7 and 8 respectively (shown in figure A.1.1). The aluminum plate with the thermistor will be laid down over the laser package. Whenever the laser package temperature changes, the aluminum plate temperature will change and consequently the thermistor resistance will change. The thermistor resistance variation with respect to temperature was given by the ILX company. **Note** that a little amount of silicon heat sink compound (DOW CORNING) was added to the contact surface between the aluminum sheet and the laser chip as well as to the contact surface between the aluminum plate and the thermistor. The heat sink compound is used in order to improve the heat transfer between the components.

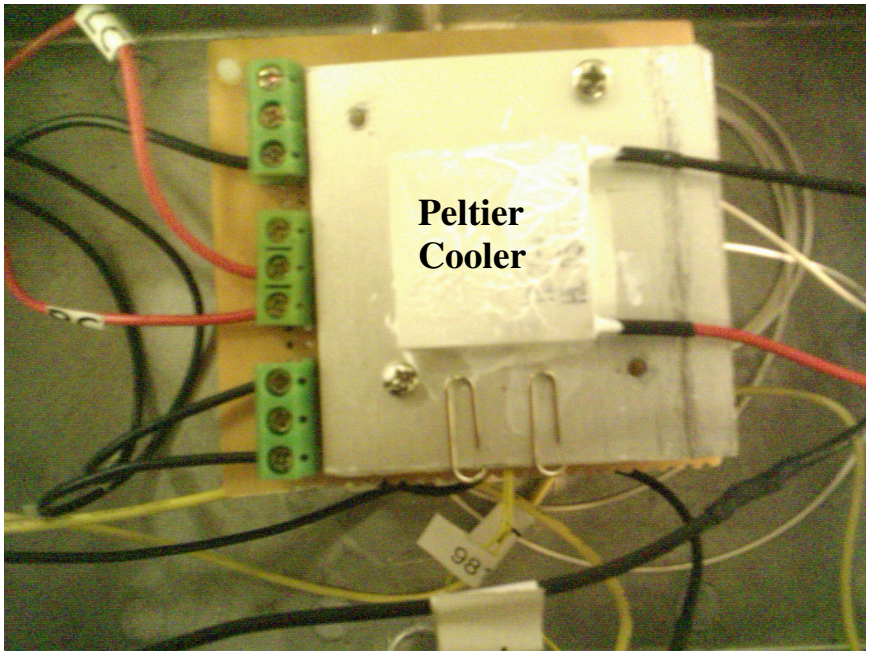

Figure A.3.2: Peltier cooler lying on the aluminum plate.

In order to control the temperature of the laser, a Peltier cooler is used. The Peltier cooler is laid on the opposite side of the aluminum plate after adding the silicon heat sink compound on the contact surface between the Peltier cooler and the aluminum plate. The Peltier cooler positive electrode (red wire) is connected to the pins (1, and 2) of the laser diode temperature controller, and the negative electrode (black wire) is connected to the pins (3, and 4) of the laser diode temperature controller. Consequently, the aluminum plate should have the thermistor at the bottom surface and the peltier cooler at the upper surface. Then, the aluminum plate is laid down with its bottom surface contacting the upper the surface of the laser diode package as shown in figure A.3.5 and A.3.6.

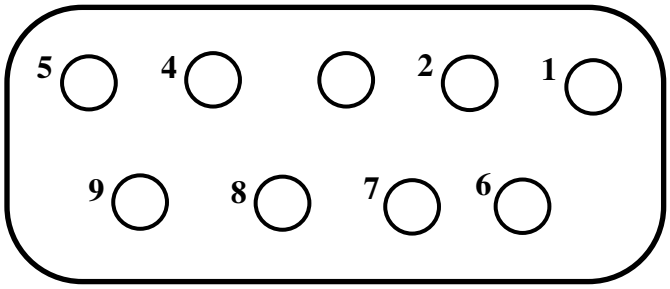

Figure A.3.3: Laser diode temperature controller back connector.

Pin Number	Pin Name
1 and 2	Peltier cooler positive electrode
3and 4	Peltier cooler negative electrode
5	Free end
6	Free end
7	Thermistor positive pin
8	Thermistor negative pin
9	Free end

Table A.3.1: Laser diode temperature controller connector numbers and their corresponding names.

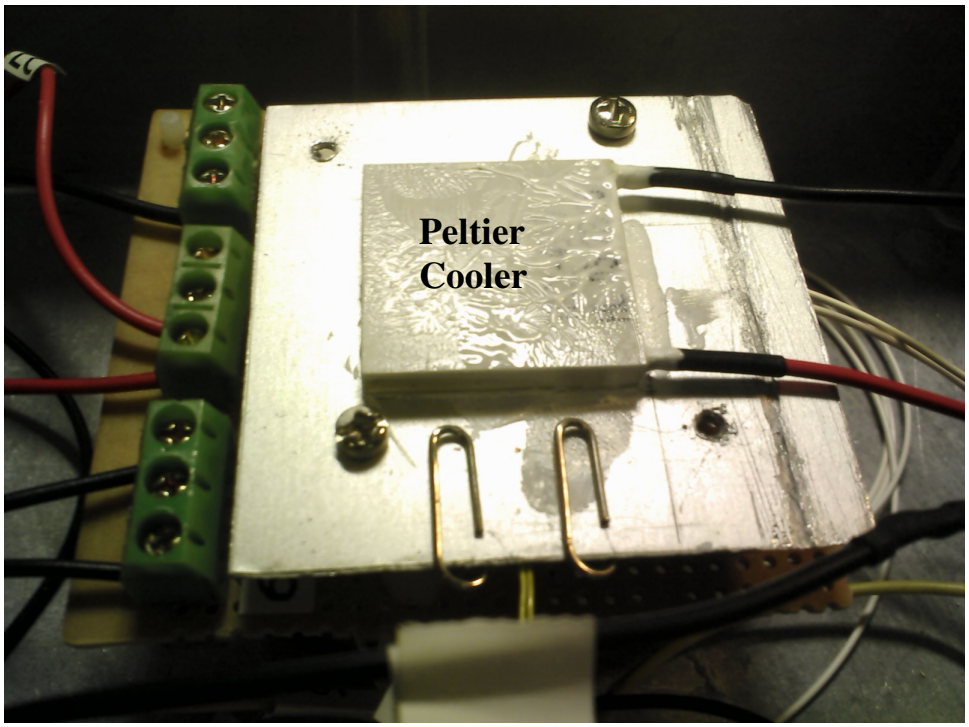

Figure A.3.4: The aluminum plate with the Peltier cooler and the thermistor laying over the laser package.

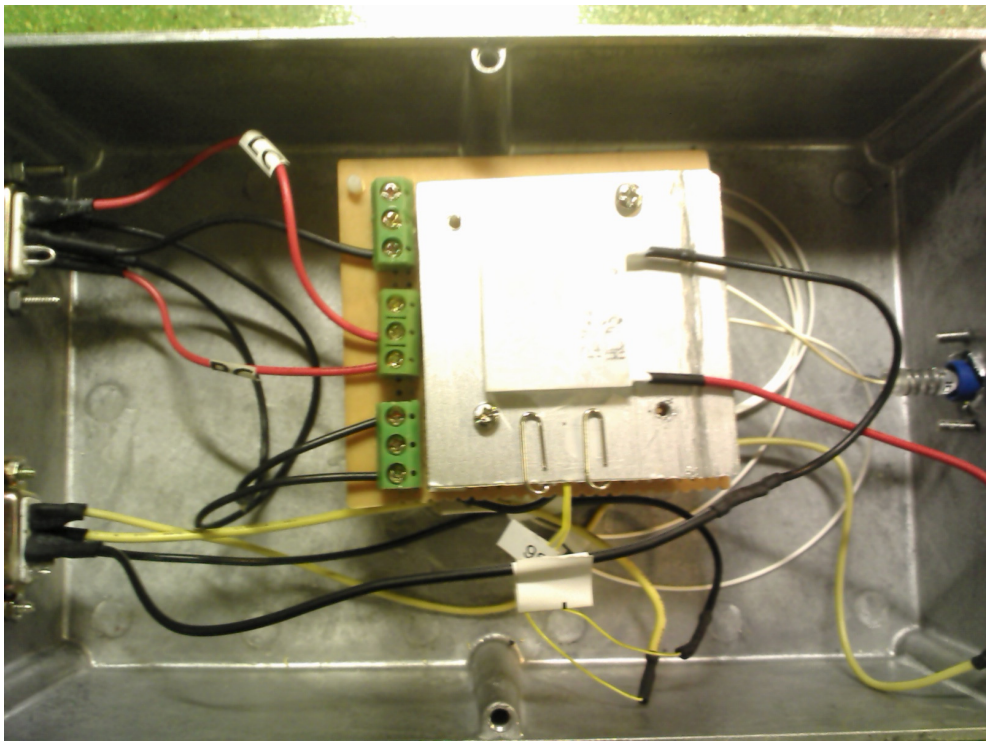

Figure A.3.5: Electrical, mechanical and optical assembly of the 1300 nm laser box.

A metallic heat sink is added to the upper surface of the Peltier cooler in order to transfer the heat from its upper surface to the surrounding as shown in figure A.3.7. A small fan can be added on top of the metallic heat sink to exchange the heat faster.

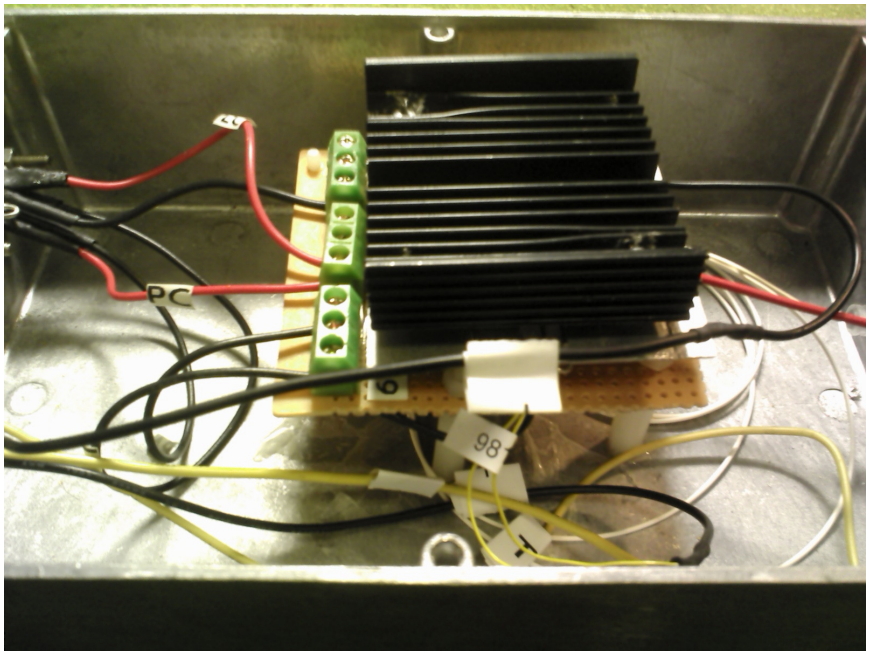

Figure A.3.6: Metallic heat sink added to the upper surface of the Peltier cooler.

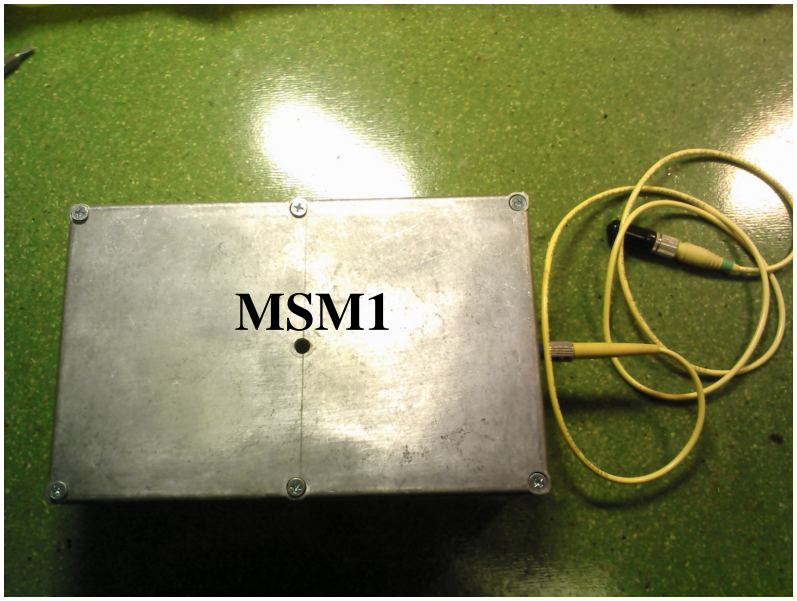

Figure A.3.7: 1300 nm AT&T laser diode box.

The temperature controller ILX LDT-5412, and current source LDX-3412 were used to operate and calibrate the 1300 nm AT&T laser diode. The 1300 nm AT&T laser diode calibration curves are shown in figure A.10. By setting the thermistor resistance value using LDT-5412, we were able to set the temperature of the Peltier cooler. By setting the temperature of the Peltier cooler, we were able to set the wavelength and the power of the 1300 nm AT&T laser diode as shown in figure A.3.9 and A.3.10.

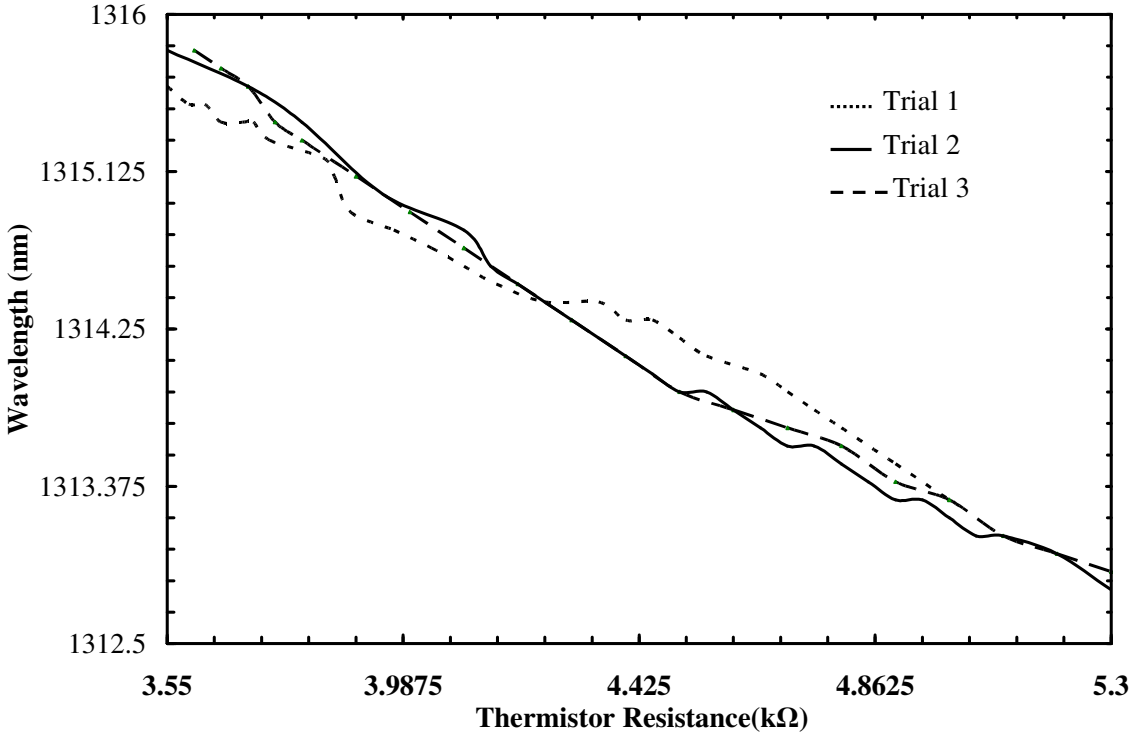

Figure A.3.8: Calibration curve of the wavelength of 1300 nm AT&T laser diode versus thermistor resistance.

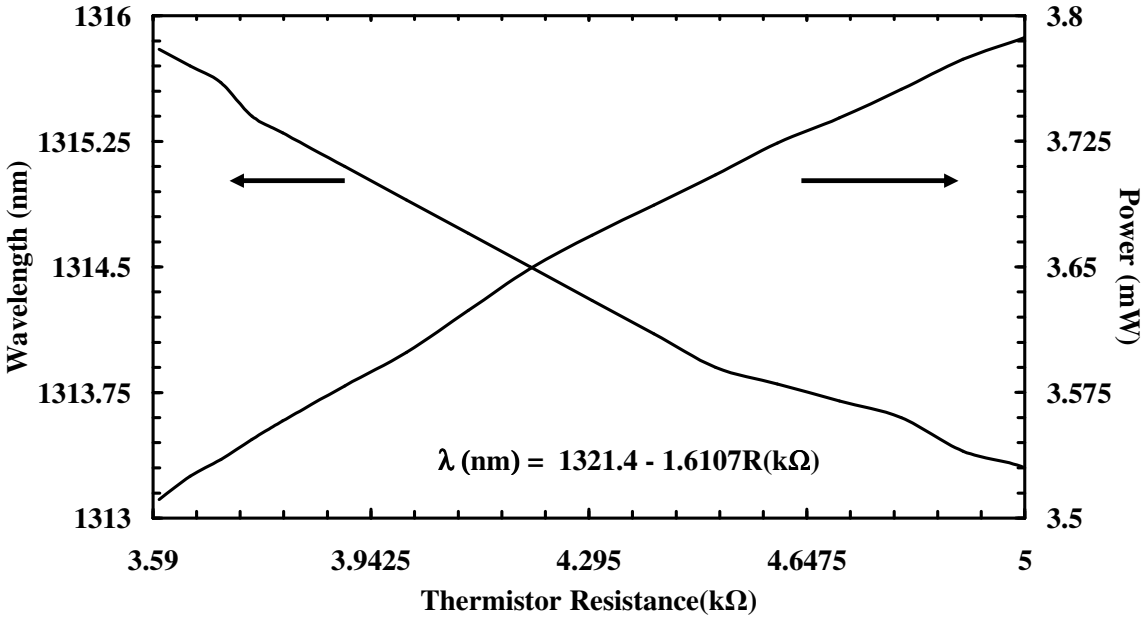

Figure A.3.9: Calibration curve of the wavelength and power of 1300 nm AT&T laser diode versus thermistor resistance.

Mohammed Sharif Murib was born in Tripoli, Lebanon in 1978. He completed the high school at Tripoli Evangelical School for Girls and Boys in 1998. He received his B.Sc. degree in Physics from Lebanese University, Faculty of Science, Hadath, Lebanon, in 2005. He joined the Modern School in Tripoli, Lebanon as high school Physics teacher for in 2005-2006. He joined International Community School in Abu Dhabi, UAE, as a high school Physics teacher. He joined the M.Sc. program in Physics at Koç University in Istanbul, Turkey in 2007, as a teaching/research assistant during which, he worked on "Resonant Cavity Enhanced Silicon Microsphere Detectors" and " High Q-factor Optical Resonances in the Elastic Scattering from Silicon Microspheres" with Prof. Ali Serpengüzel. As of fall 2009, he will continue his Ph.D. work at Koç University. He is expected to work with Prof. Hakan Ürey on "Biosensors'' and "Optical Interconnection".